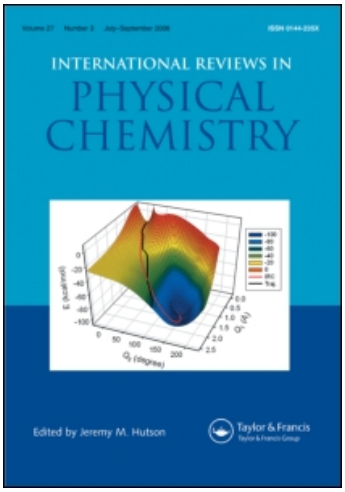

International Reviews in Physical Chemistry
Publication details, including instructions for authors and subscription information:
http://www.informaworld.com/smpp/title~content=t713724383

Magnetic circular dichroism for surface and thin film magnetism: Measurement techniques and surface chemical applications

Toshihiko Yokoyama[a]; Takeshi Nakagawa[a]; Yasumasa Takagi[a]
[a] Department of Materials Molecular Science, Institute for Molecular Science and Department of Structural Molecular Science, The Graduate University for Advanced Studies (Sokendai), Okazaki, Aichi 444-8585, Japan

To cite this Article Yokoyama, Toshihiko , Nakagawa, Takeshi and Takagi, Yasumasa(2008) 'Magnetic circular dichroism for surface and thin film magnetism: Measurement techniques and surface chemical applications', International Reviews in Physical Chemistry, 27: 3, 449 — 505
To link to this Article: DOI: 10.1080/01442350802127608
URL: http://dx.doi.org/10.1080/01442350802127608

International Reviews in Physical Chemistry
Vol. 27, No. 3, July–September 2008, 449–505

Taylor & Francis
Taylor & Francis Group

REVIEW ARTICLE

Magnetic circular dichroism for surface and thin film magnetism: Measurement techniques and surface chemical applications

Toshihiko Yokoyama*, Takeshi Nakagawa and Yasumasa Takagi

Department of Materials Molecular Science, Institute for Molecular Science and Department of Structural Molecular Science, The Graduate University for Advanced Studies (Sokendai), Myodaiji-cho, Okazaki, Aichi 444-8585, Japan

(*Received 5 March 2008; final version received 6 April 2008*)

The technical development of the characterization of magnetic thin films is an urgent subject especially for further improvement of high-density and high-speed recording media. This article focuses attention on the fundamental methodology and recent exploitations of various magnetic circular dichroism (MCD) techniques. First, basic theories and experimental methods of the magneto-optical Kerr effect (MOKE) and X-ray magnetic circular dichroism (XMCD) are described. MOKE is a conventional but usually the most useful method to characterize macroscopic magnetization of metal thin films using visible lasers. Moreover, recent development of MOKE allows one to perform optical microscopic and ultrafast time resolved investigations. XMCD has now become a mature technique by virtue of the developments of soft and hard X-ray synchrotron radiation sources. Since XMCD is based on core absorption spectroscopy, the technique provides information on element specific magnetization. Using the so-called sum rules, one can determine the microscopic spin and orbital magnetic moments. The experimental method and an example using a superconducting magnet system combined with a liquid helium sample cryostat are described. Moreover, by combining XMCD with photoelectron emission microscopy (PEEM), one can perform spatiotemporal measurements, whose spatial resolution reaches several tens of nanometres. Magnetization induced second harmonic generation (MSHG) is also described. This is a unique technique for its inherently high sensitivity to surfaces and interfaces since MSHG is inhibited in the bulk of centrosymmetric crystals. The drastic polarization dependence of MSHG based on the selection rules is also discussed. As a last method addressed in this article, the threshold photoemission MCD technique is reviewed. The technique has recently been proposed and has demonstrated the possibility of an ultrafast spatiotemporal method by combining PEEM. Applications of these various MCD families to surface physical chemistry are described. Here, drastic spin reorientation transitions (SRT) of some metal thin films induced by adsorption of atoms and molecules are discussed from the macroscopic and microscopic points of view. Consequently, future aspects in the MCD techniques and surface and thin film magnetism are addressed.

Keywords: magnetic circular dichroism (MCD); magneto-optical Kerr effect (MOKE); X-ray magnetic circular dichroism (XMCD); magnetization induced second harmonic generation; photoemission magnetic circular dichroism; spin reorientation transition (SRT); magnetic anisotropy

*Corresponding author. Email: yokoyama@ims.ac.jp

ISSN 0144–235X print/ISSN 1366–591X online

DOI: 10.1080/01442350802127608
http://www.informaworld.com

Contents PAGE

1. Introduction

The Nobel Prize in Physics for 2007 was awarded jointly to Albert Fert and Peter Grünberg, who independently discovered in 1988 the totally new physical effect of giant magneto-resistance (GMR) in Fe/Cr/Fe thin layers [1,2]. A GMR system of this kind is a perfect tool for reading data from hard disks when information registered magnetically has to be converted to electric current. In 1997, the first read-out head based on the GMR effect was launched and this soon became the standard technology. The period between the first scientific discovery of the GMR effect and the realization of commercial applications was astonishingly short. Besides the discoveries of outstanding spintronic phenomena such as GMR and TMR (tunnelling magneto-resistance) effects as well as the spin-torque effect, our knowledge and understanding of the fundamental properties of magnets have dramatically increased in these decades. Developments of quantum-mechanical theories and simulations are attributed to one of the most important areas of progress: accurate many-body electronic structure calculations of magnetically ordered ground and excited states, and reliable theoretical simulations of micromagnetic structures and magnetic dynamics on nano- and micromagnetic scales have been realized. Moreover, in the field of materials science, various kinds of novel magnets with extraordinary physical properties were discovered: diluted ferromagnetic semiconductors, half-metallic Heusler alloys, heavy Fermion systems, magnetocaloric and magnetic shape memory alloys, etc. This outstanding progress is substantially owed to recent developments of information technology and nanotechnology. Here, we will also recall that the Nobel Prize in Chemistry for 2007 was awarded to Gerhard Ertl for his groundbreaking studies concerning surface science in an ultrahigh vacuum (UHV) condition. Needless to say, many UHV surface science techniques are closely related to the field of thin film magnetism. We will again attribute this important progress to advanced material preparation techniques such as molecular beam epitaxy, sputtering, nanoprocessing, self-assembling, etc. and the exploitation of various novel UHV measuring methods that allow profound characterization of magnetic properties.

Various kinds of sophisticated characterization techniques have been developed for the investigations of thin film magnetization: X-ray and neutron diffraction, Lorentz microscopy and electron holography, spin-polarized photoemission spectroscopy, ferromagnetic resonance (FMR), and scanning probe microscopy (SPM) as magnetic force microscopy (MFM) and spin-polarized scanning tunnelling microscopy (SP-STM), and magnetic circular dichroism (MCD) [3]. In this article, we will discuss the MCD technique in detail as one of the most suitable methods for the investigation of thin film magnetization. The MCD technique has a range of X-ray magnetic circular dichroism (XMCD) using synchrotron radiation X-rays, the magneto-optical Kerr effect (MOKE) using UV-visible light, magnetization induced second harmonic generation (MSHG) using short pulsed lasers, and so forth. A related method based on magnetic linear dichroism (MLD) can also be included. These MCD methods have several advantages and disadvantages compared to the other techniques. The MCD methods are rather easily conducted under UHV and applied magnetic field conditions, especially as MOKE does, since photons are used as a probe and a detector does not have to be rotated as in the case of diffraction. Even in the case of the electron detection mode in XMCD, the externally applied magnetic field does not affect the data collection as photoemission measurements, because the electron energies are not necessarily analysed. Second, since the pulsed light

can be used as a probe, fast spin dynamics can be investigated. Especially, using ultrashort pulsed lasers one can investigate femtosecond spin dynamics, which is going to be important for the further exploitation of high-density high-speed magnetic recording media. Third, XMCD has the unique feature of element specificity and moreover provides information on both spin and orbital magnetic moments separately. This is in good contrast to SQUIDs (Superconducting Quantum Interference Devices) which are the most popular technique in studies of bulk magnets and measures a total absolute quantity of magnetization, sometimes including inevitable impurity contributions. Fourth, MOKE can be applied to microscopy as an optical polarization microscope with special resolution down to the diffraction limit. When MOKE is combined with a scanning near-field optical microscope (SNOM), one can overcome the diffraction limit to yield a special resolution of <100 nm, although to our knowledge no UHV-compatible SNOM-MOKE has been reported so far. XMCD is more easily applied to nanoscale microscopy by combining photoelectron emission microscopy (PEEM) with a special resolution of <50 nm. Fifth, MSHG also has the unique feature that the surface and interface magnetization is investigated because the bulk contribution to SHG is strictly inhibited in centrosymmetric magnetic materials. MSHG is again suitable to ultrafast time-resolved experiments since it inherently requires ultrashort pulsed lasers. In Sections 2–4, we will review the basic theories, experimental methods and recent progress of these MCD families in detail.

In Section 5, we will review a novel method of threshold photoemission MCD [4,5]. The MCD in the UV–visible regions is usually quite small because of the far smaller spin–orbit interaction in the valence bands than that in the core shells that are excited in XMCD. In fact, Marx *et al.* [6] investigated MLD using PEEM with a Hg lamp. They observed only 0.19% MLD asymmetry from a thick (100 nm) Fe film, which is reasonably comparable to the MOKE one, while the trial of a MCD PEEM measurement failed due to too weak intensities. It was thus believed that UV MCD PEEM is not practically useful because of its too weak sensitivity and that XMCD PEEM using third generation synchrotron radiation light sources has to be utilized for the investigation of nanostructure magnetism. Nakagawa and Yokoyama [4], however, discovered significantly enhanced MCD in the vicinity of the work function threshold. Surprisingly, the threshold photoemission MCD asymmetry is found to be as much as two orders of magnitude stronger than the usual MOKE asymmetry in the UV region and to give a comparable intensity to XMCD. More than 10% MCD asymmetry was observed in perpendicularly magnetized $\sim$10 monolayer (ML) Ni grown epitaxially on Cu(001) when the photon energy was tuned to the work function threshold. Subsequently, Nakagawa *et al.* [5] succeeded in the observation of beautiful UV MCD PEEM images. While XMCD PEEM requires third generation synchrotron radiation light sources, UV MCD PEEM could be measured in the laboratory using UV lasers. Moreover, when one uses ultrashort pulsed lasers, the time resolving power may easily reach $\sim$100 fs, which is around three orders of magnitude faster than that of synchrotron radiation experiments.

Section 6 deals with examples of applications of the MCD techniques, where thin film magnetism is reviewed from the view point of surface science. The important subject in the combination between thin film magnetism and surface science can be found in the substantial change of magnetic properties of thin films induced by surface chemical control such as adsorption and desorption of atoms and molecules. An excellent example

can be seen in Ni/Cu(001); when hydrogen is atomically adsorbed on the surface of in-plane magnetized 7–9 ML Ni/Cu(001), the whole system undergoes a spin reorientation transition (SRT) into perpendicular magnetic anisotropy (PMA) [7]. While the adsorption takes place only at the surface and there should be no interaction between the adsorbate and the inner Ni layers, the drastic SRT abruptly occurs for the whole Ni film. Such a drastic macroscopic phenomenon might not be found in any other macroscopic effect induced by surface adsorption. For the understanding of such a drastic change in magnetic anisotropy, XMCD is one of the most suitable methods since it provides information on orbital magnetic moments. The exchange interaction that is the origin of ferromagnetism is basically isotropic and cannot explain magnetic anisotropy. The spin–orbit interaction which is far smaller than the exchange interaction may play a dominant role for the determination of magnetic easy and hard axes. The quantitative estimation of orbital magnetic moments by means of XMCD could provide microscopic understanding of the SRT induced by atomic and molecular adsorption. The present article reviews several examples of adsorbate induced SRT studied by XMCD and other techniques in details. Finally, concluding remarks and some future prospects will briefly be discussed in Section 7.

2. Magneto-optical Kerr effect (MOKE)

In order to investigate magnetic properties of thin films, the magneto-optical Kerr effect (MOKE) [3,8–13] technique is the most basic and standard method. When linearly polarized light is reflected by magnetized matter, the electric field vector of the reflected light is rotated with respect to that of the incident one. A similar optical rotation is observed in the transmission mode, which is called the magneto-optical Faraday effect [10], although the MOKE is usually more important for the investigation of magnetic thin films due to no transparency. In MOKE measurements, there typically exist three different configurations as shown in Figure 1. When the magnetization is perpendicular to the films surface, the configuration is called *polar* MOKE configuration (left panel in Figure 1). On the other hand, when the magnetization is parallel to the film surface and is within the light reflection plane, the configuration is named *longitudinal* MOKE (middle panel). In the polar MOKE configuration, the Kerr rotation angle is usually more than one order of magnitude greater than that of the longitudinal case for equivalent samples. Such a huge and essential difference between polar and longitudinal MOKE will be discussed below. The third configuration is the *transverse* MOKE geometry, where the magnetization is parallel to the surface and is perpendicular to the reflection plane (right panel). In this configuration, the Kerr rotation or ellipticity is not observable, while the intensity

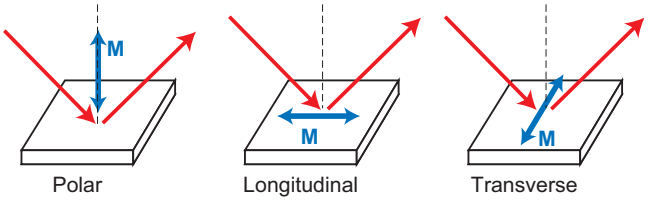

Figure 1. [Colour online] Typical configurations of polar, longitudinal and transverse MOKE.

of the reflectivity can be a measure of the magnetization. In the polar and longitudinal MOKE geometries, the Kerr rotation angle is described as a complex quantity as in the case of other optical quantities like dielectric constants and reflectivities. The imaginary part of the Kerr rotation angle corresponds to the Kerr ellipticity or MCD. The Kerr rotation angle and ellipticity are not independent of each other due to the strict validity of the Kramers–Kronig theorem. In this section, the basic principle and the experimental methods of MOKE will be described [14].

2.1. *Phenomenological theory of MOKE*

Before discussing the magneto-optical effect, we will first recall the definition of circular polarization [15]. Although the words *left* and *right* are often used to distinguish the circular polarization, they are confusing because the definition of left and right clearly depends on the direction from which we observe the light. In this sense, the definition using the *helicity* is strongly recommended. Let us assume that the light is propagating from the $-z$ to $+z$ direction and the electric field vector $\mathbf{E}(t, z)$ is given by

$$\mathbf{E}(t, z) = \mathbf{E}_0 \exp[-\mathrm{i}(\omega t - kz)] = \mathbf{E}_0 \exp\left[-\mathrm{i}\left(\omega t - \frac{N}{c} z\right)\right], \tag{1}$$

where t is the time, ω the frequency, $k = N/c$ the wavenumber (N the refractive index and c the velocity of light), and $\mathbf{E}_0$ is the time- and space-independent constant of the electric field vector. There exist two kinds of circularly polarized light that can be defined as

$$\mathbf{E}^{\pm}(t, z) = \mathbf{E}_0^{\pm} \exp[-\mathrm{i}(\omega t - kz)] \quad \text{and} \quad \mathbf{E}_0^{\pm} = \frac{E_0}{\sqrt{2}}(\mathbf{e}_x \pm \mathrm{i}\mathbf{e}_y). \tag{2}$$

As can be seen in Figure 2, both of the $\mathrm{Re}[\mathbf{E}^{\pm}(t = 0, z = 0)]$ vectors are directed towards $+x$, while $\mathrm{Re}[\mathbf{E}^{\pm}(t = \pi/2\omega, z = 0)]$ rotate to the $\pm y$ directions, respectively. The helicity h is defined as a projection of the angular momentum $\boldsymbol{\sigma}$ of the light onto the wavevector $\boldsymbol{k}$; namely, $h = \sigma \cdot \hat{\mathbf{k}}$, where $\hat{\mathbf{k}}$ is the unit vector of the wavevector $\mathbf{k}$. The perfect circularly polarized light defined by $\mathbf{E}_0^+$ and $\mathbf{E}_0^-$ thus corresponds to positive ($h = +1$) and negative ($h = -1$) helicities, respectively. When we look at the rotation of $\mathbf{E}^{\pm}(t, z = 0)$ from the $-z$ to $+z$ direction, the positive and negative helicity light rotates clockwise (*right*) and counter-clockwise (*left*), respectively. This is the standard definitions for *left* and *right* in the magneto-optical theory [15]. Moreover, we can recognize that the definition of the circular polarization factor P_c is identical to that of the helicity:

$$P_c \equiv \frac{|\mathbf{E}_0^+|^2 - |\mathbf{E}_0^-|^2}{|\mathbf{E}_0^+|^2 + |\mathbf{E}_0^-|^2} = h = \boldsymbol{\sigma} \cdot \hat{\mathbf{k}}. \tag{3}$$

Care should also be taken of the relation between the light-propagating z axis and the quantized Z axis of the system that will be used below.

Let us next describe the phenomenological relationship between the dielectric constant and the Kerr rotation angle. Although the detailed derivation of the formula is omitted here, one can find the description in many textbooks and literature on magneto-optics [11–14]. Consider an isotropic magnetic material with a magnetization

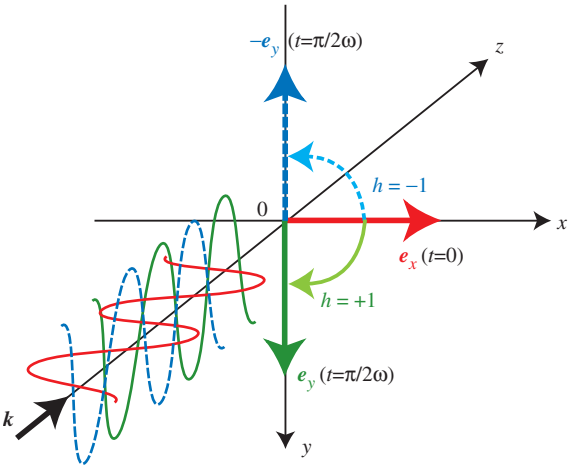

Figure 2. [Colour online] Definition of the circular polarization based on the helicity. At $t=0$ and $z=0$, the electric field vector **E** points to the $+x$ direction. At $t=\pi/2\omega$ and $z=0$, **E** is directed to $\pm y$ for the positive and negative helicity light, respectively. In the magneto-optical theory, the positive (negative) helicity light, whose electric field vector **E** rotates clockwise (counter-clockwise) when one sees from the $-z$ to $+z$ direction, is called right (left) circular polarization.

M parallel to the $\pm z$ axis, for simplicity (**M**//**k**//z). The dielectric constant $\boldsymbol{\epsilon}$ of the magnetic material is given as a tensor

$$\boldsymbol{\varepsilon} = \begin{pmatrix} \varepsilon_{xx} & \varepsilon_{xy} & 0 \\ \varepsilon_{xy} & \varepsilon_{xx} & 0 \\ 0 & 0 & \varepsilon_{zz} \end{pmatrix}, \tag{4}$$

where $\boldsymbol{\varepsilon}$ is in general a complex quantity. According to classical electromagnetic theory, the Maxwell equations give the second-order differential equation concerning **E** as

$$\nabla \times \nabla \mathbf{E} + \varepsilon \frac{\partial}{\partial t} \mathbf{E} = 0. \tag{5}$$

Here, we assume the magnetic permeability of $\mu = \mu_0$ (μ_0 the permeability of vacuum) in UV–visible light, where the frequency is too fast for the material to respond magnetically. By substituting **E** in Equation (5) with Equation (1), we will reach an eigenvalue problem, in which the secular equation is given as

$$\begin{vmatrix} N^2 - \varepsilon_{xx} & \varepsilon_{xy} & 0 \\ \varepsilon_{xy} & N^2 - \varepsilon_{xx} & 0 \\ 0 & 0 & N^2 - \varepsilon_{zz} \end{vmatrix} = 0. \tag{6}$$

The eigenvalues and the eigenfunctions are obtained as

$$N_{\pm}^2 = \varepsilon_{xx} \pm \mathrm{i}\varepsilon_{xy}, \tag{7}$$

and

$$\mathbf{E}^{\pm} = E_0(\mathbf{e}_x \pm \mathrm{i}\mathbf{e}_y)\exp\left[-i\omega\left(t - \frac{N_{\pm}z}{c}\right)\right] \tag{8}$$

Both of the circular polarizations expressed as Equation (2) are found to be eigenstates in the magnetic material. The difference of N between the positive and negative helicity light, $\Delta N = N_+ - N_-$, is evaluated from Equation (7):

$$\Delta N = \frac{\mathrm{i}\varepsilon_{xy}}{\sqrt{\varepsilon_{xx}}}. \tag{9}$$

One can understand that the MCD in the refractive index is proportional to the off-diagonal element ϵ_{xy} and is also dependent on the diagonal element $\varepsilon_{xx}^{-1/2}$.

The complex reflectivity (the Fresnel coefficient) $r_{\pm}$ for the positive and negative helicity light is given as $r_{\pm} = (N_{\pm} - 1)/(N_{\pm} + 1)$, where the light is assumed to propagate in vacuum. The complex Kerr rotation Φ_K is consequently expressed as a function of the Fresnel coefficient:

$$\Phi_K = \theta_K + \mathrm{i}\eta_K \cong \frac{\mathrm{i}}{2}\ln\frac{r_-}{r_+}. \tag{10}$$

Since the Kerr rotation angle is dependent on the incident and reflected angles and cannot be given as a universal form, the formula for the normal incidence polar Kerr geometry can be simply described, assuming that both the light wavevector and the magnetization are parallel to the z axis:

$$\Phi_K \cong \frac{\varepsilon_{xy}}{(1 - \varepsilon_{xx})\sqrt{\varepsilon_{xx}}}. \tag{11}$$

The MOKE is also dependent not only on the off-diagonal element ϵ_{xy} but on the diagonal element ϵ_{xx}. The Kramers–Kronig relation holds between the Kerr rotation θ_K and the Kerr ellipticity η_K:

$$\theta_K(\omega) = \frac{2}{\pi}\mathcal{P}\int_0^{\infty}\frac{\omega'\eta_K(\omega')}{\omega'^2 - \omega^2}\mathrm{d}\omega' \tag{12}$$

and

$$\eta_K(\omega) = \frac{2\omega}{\pi}\mathcal{P}\int_0^{\infty}\frac{\theta_K(\omega')}{\omega'^2 - \omega^2}\mathrm{d}\omega', \tag{13}$$

where $\mathcal{P}$ denotes the principal integral.

At the end of this subsection, we will consider the reason why the polar MOKE is typically more than one order of magnitude stronger than the longitudinal MOKE. The magneto-optical interaction is proportional to $\hat{\mathbf{M}} \cdot P_c\hat{\mathbf{k}}$. When the incident angle of the light θ_{in} is 45°, the absolute value of the scalar product $\hat{\mathbf{M}} \cdot P_c\hat{\mathbf{k}}$ does not differ between the polar and longitudinal configurations. Actually, as described in the next section, the XMCD intensity is strictly proportional to the scalar product of $\hat{\mathbf{M}} \cdot P_c\hat{\mathbf{k}}$. The reason for the huge difference in MOKE is the presence of the reflected light. This can be easily

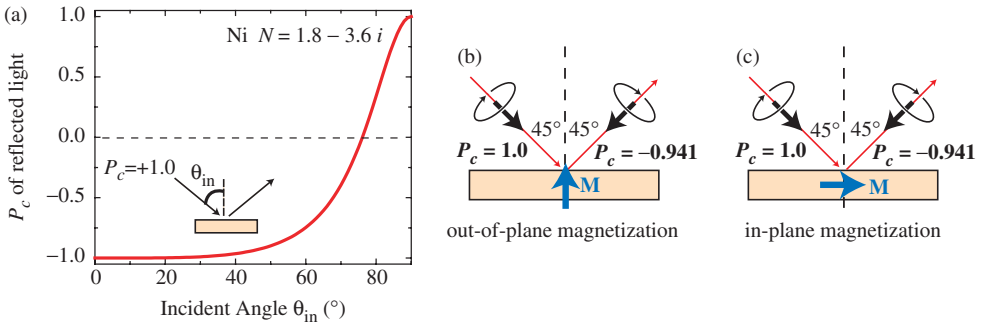

Figure 3. [Colour online] (a) Circularly polarization factor P_c (helicity) of the reflected light from bulk Ni (the refractive index $N = 1.8-3.6i$) as a function of the incidence angle θ_{in}. (b), (c) Geometrical relation between the photon angular momentum $P_c\hat{\mathbf{k}}$ (black arrows) and magnetization $\mathbf{M}$ (blue arrows) in the polar (b) and longitudinal (c) MOKE configurations. One can immediately find that the presence of the reflected light enhances the polar MOKE while it cancels the longitudinal one.

understood from Figure 3. Figure 3(a) depicts the circular polarization factor P_c of the reflected light when the incidence light with $P_c = +1.0$ is irradiated on Ni with the incidence angle θ_{in}. It is apparent that the sign of P_c is reversed for the wide range of the incidence angle. The Brewster angle that gives perfectly S-polarized reflection with $P_c = 0$ is as much as 76.6°. The $\theta_{in} = 45°$ incidence angle provides $P_c = -0.941$. Figures 3(a) and (b) show the relationship between $\mathbf{M}$ and $P_c\hat{\mathbf{k}}$ for the polar and longitudinal configurations, respectively. It is easily understood from the directions of $P_c\hat{\mathbf{k}}$ that the reflected light enhances the magneto-optical interaction in the polar MOKE configuration, while it cancels in the longitudinal configuration. Although the reflectivity is not included in Figures 3(a) and (b), the reason for the huge difference of the MOKE intensity between the polar and longitudinal configurations is apparent. In the XMCD measurements, there exists no reflected light except for an extreme grazing incidence geometry, leading to a simple XMCD intensity proportional to $\hat{\mathbf{M}} \cdot P_c\hat{\mathbf{k}}$.

2.2. *Quantum-mechanical theory of MOKE*

The dielectric constant is characterized by quantum-mechanical theory [16]. Although the strict derivation of the dielectric constant should be performed by using the Kubo formula [17], this can be referred to in the literature [18–21] and a simple derivation will be described here for easier understanding of the phenomena. Based on the perturbation theory of the time-dependent Schrödinger equation, the electron polarization $\mathbf{P}$ can be evaluated, as can be seen in many quantum-mechanical textbooks. We will here define the electric field vector of the linearly polarized light as $\mathbf{E} = \mathbf{E}_0(\exp[-i\omega t] + \exp[i\omega t])$. By assuming the electric dipole approximation, the expectation value of the x component of the polarization $\mathbf{P}$ is given as

$$\langle P_x \rangle = \langle nex(t) \rangle = ne^2 \left[\sum_j \frac{x_{j0}^2}{\hbar} \left(\frac{1}{\omega_{j0} - \omega} + \frac{1}{\omega_{j0} + \omega} \right) \right] E_x(t), \tag{14}$$

where n is the electron density, $\hbar$ the Planck constant divided by 2π, e the elementary charge, $ex_{j0} = e\ \langle j|x|0\rangle$ is the x component of the electric dipole induced between the ground state 0 and the excited state j, and $\hbar\omega_{j0}$ is the transition energy between the states 0 and j. Here, only the linear response is taken into account, and the distribution function for the electron occupation is neglected. By using the relation of $\mathbf{D} = \epsilon\mathbf{E} = \epsilon_0\mathbf{E} + \mathbf{P}$ ($\mathbf{D}$ the electric displacement vector and ϵ_0 the dielectric constant of vacuum), we obtain

$$\varepsilon_{xx}(\omega) = 1 + \frac{ne^2}{m\varepsilon_0}\sum_j f_{xj}\frac{1}{\omega_{j0}^2 - (\omega + \mathrm{i}/\tau)^2}, \tag{15}$$

where m the electron mass and τ the relaxation time. f_{xj} is the x component of the oscillator strength upon the transition between the states 0 and j, given as

$$f_{xj} = \frac{2m\omega_{j0}}{\hbar}|x_{j0}|^2. \tag{16}$$

The off-diagonal element of the dielectric constant ϵ_{xy} is evaluated from the expectation value of the polarization P_x in an electric field along the y axis. $\langle P_x\rangle$ is given as

$$\langle P_x\rangle = \langle nex(t)\rangle = ne^2\left[\sum_j \frac{x_{j0}y_{0j}}{\hbar}\left(\frac{E_{y0}^*\exp(-i\omega t)}{\omega_{j0} - \omega} + \frac{E_{y0}\exp(i\omega t)}{\omega_{j0} + \omega}\right)\right]. \tag{17}$$

The off-diagonal dielectric constant is consequently obtained as the susceptibility for the electric field $\exp[-\mathrm{i}\omega t]$:

$$\varepsilon_{xy}(\omega) = -\frac{ne^2}{2m\varepsilon_0}\sum_j \frac{f_{xj}^+ - f_{xj}^-}{\omega_{j0}^2 - (\omega + \mathrm{i}/\tau)^2} \tag{18}$$

where f_{xj}^+ and f_{xj}^- are the oscillator strengths for the light with positive and negative helicities as

$$f_{xj}^{\pm} = \frac{m\omega_{j0}}{\hbar}|x_{j0}^{\pm}|^2, \tag{19}$$

and $ex_{j0}^{\pm}$ are the electric dipole elements for the positive/negative helicity light. It is apparent that the off-diagonal element $\epsilon_{xy}(\omega)$ includes the difference of the absorption intensity between the positive and negative helicity light.

In order to understand the origin of MCD, let us consider a simple transition from the s- to p-type orbitals, as depicted in Figure 4. In the ground state, one electron occupies the s orbital, while the p orbital is completely vacant. Without the magnetization, either the $s\alpha$ or $s\beta$ orbitals are occupied equivalently and no MCD can be seen (the first panel on the left in Figure 4), although the $s \to p$ transition is dipole allowed. In the presence of the exchange interaction (or the Zeeman splitting), the $s\alpha$ or $s\beta$ orbitals are energetically separated, leading to inequivalent occupation in the $s\alpha$ or $s\beta$ spin orbitals, as in the second panel from the left in Figure 4. The MCD is nevertheless not observed, since both the positive and negative helicity light excite the $s\alpha$ electron to the $p\alpha$ level equivalently.

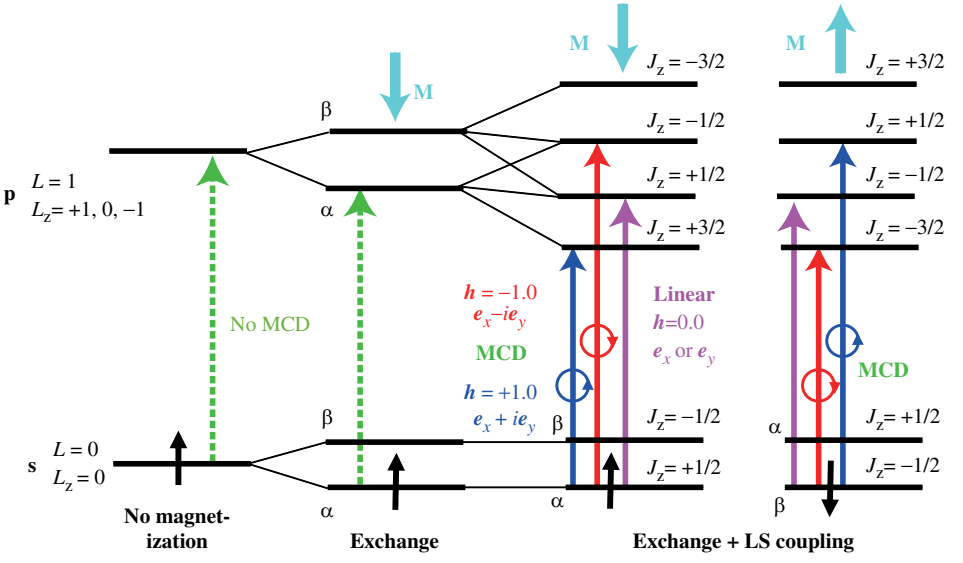

Figure 4. [Colour online] Origin of the magneto-optical effect concerning the *s*-to-*p* transition. When the system has no magnetization or only the exchange interaction, no magnetic circular dichroism can be observed (see the left two panels). In the presence of both the exchange interaction (magnetization) and the spin–orbit interaction, MCD appears due to the splitting of the *p* orbital (see the right two panels). The helicity switching is substantially identical to the magnetization switching. From [14].

When the spin–orbit coupling is added, however, the energy levels are further split in the *p* orbitals, as in the third panel of Figure 4. In the *LS* coupling scheme, the *p* orbital exhibits four levels depending on the J_z value ($J_z = -3/2$, $-1/2$, $1/2$ and $3/2$). The positive helicity light of $\mathbf{E}^+ \propto \boldsymbol{e}_x + \mathrm{i}\boldsymbol{e}_y$ induces the transition of $\Delta J_z = +1$; namely, the transition from $J_z = 1/2$ to $J_z = 3/2$ is allowed. On the contrary, with the negative helicity light of $\mathbf{E}^- \propto \boldsymbol{e}_x - \mathrm{i}\boldsymbol{e}_y$, the transition from $J_z = 1/2$ to $J_z = -1/2$ ($\Delta J_z = 1$) is allowed. Since the excitation energies and the transition probability from $J_z = 1/2$ to $J_z = -1/2$ and $3/2$ are different from each other, MCD should appear. Note also that when the linear polarization is used ($\mathbf{E} \propto \boldsymbol{e}_x$ or $\boldsymbol{e}_y$), the transition from $J_z = 1/2$ to $J_z = 1/2$ ($\Delta J_z = 0$) is allowed. The fourth panel in Figure 4 depicts the reversal of magnetization with respect to the third one. In this case, the positive helicity light induces the transition from $J_z = -1/2$ to $J_z = +1/2$, while negative helicity light induces the transition from $J_z = -1/2$ to $J_z = -3/2$. It is noted from the right two panels in Figure 4 that magnetization reversal is essentially identical to helicity switching. One can consequently understand that MCD requires *both* spin polarization *and* spin–orbit coupling. This is in good contrast to spin-polarized photoemission, which is observable if the system shows *either* spin polarization *or* spin–orbit coupling. In the presence of spin polarization, light polarization is not required (any polarization or non-polarized light gives spin polarized photoemission). In the diamagnetic system with spin–orbit splitting, we can detect spin polarized photoemission by using circularly polarized light. A typical well-known example is diamagnetic GaAs and related materials, which are excellent spin polarized electron sources under irradiation of the circularly polarized laser.

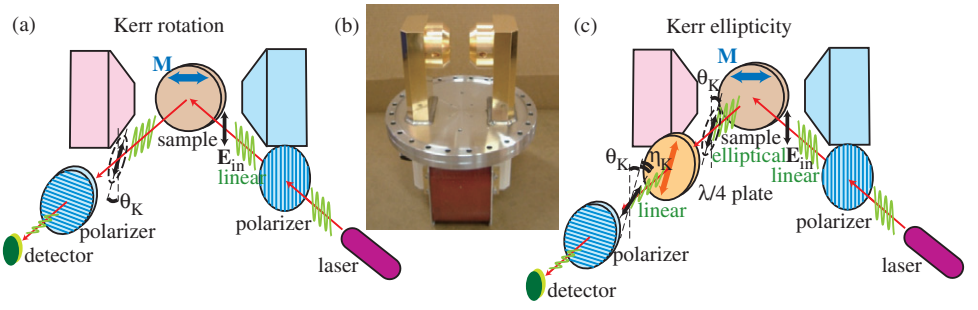

Figure 5. [Colour online] Experimental setup of the (a) Kerr rotation and (c) Kerr ellipticity measurements. A photo of a UHV compatible electromagnet is also given in (b).

2.3. *Experimental setup of MOKE*

The experimental setup of MOKE is rather simple [21]. When one wants to measure only magnetization curves without the dependence of the photon energy, diode lasers can be used as a light source. Figures 5(a) and (c) show the experimental longitudinal MOKE setups for the Kerr rotation and ellipticity measurements, respectively. Laser light that is linearly polarized by the first polarizer is reflected by a sample in a magnetic field. The Kerr rotation angle θ_K can be measured by placing another polarizer in the crossed nicols configuration. The intensity of the stray light, which is detected by a photodiode, is proportional to the Kerr rotation angle. The polar MOKE setup is similar, although the magnetic field or the magnetization is perpendicular to the sample surface. A photograph of a typical UHV electromagnet is depicted in Figure 5(b). In order to suppress heating of the coil that leads to possible worsening of the pressure, the coil is placed outside. The yoke and poles are made of pure Fe coated with gold inside the vacuum. When the pole–pole distance is 35 mm, we can obtain a maximum magnetic field of ~3000 Oe, which is usually sufficient for the magnetization along the magnetic easy axes.

The Kerr ellipticity η_K can be measured by placing a quarter-wave plate between the sample and the detecting polarizer. When the fast axis of the quarter-wave plate is set parallel to the short axis of the elliptically polarized light, the light transmitted from the quarter-wave plate is linearly polarized with the electric field vector rotating by η_K with respect to that of the reflected light, namely rotating approximately by $\theta_K + \eta_K$ with respect to that of the incidence light. The intensity of the stray light from the detecting polarizer is also proportional approximately to $\theta_K + \eta_K$.

Recent progress in MOKE, such as optical microscopy and ultrafast spin dynamics, can be found in textbooks [3]. Although the present review omits the subject, several applications of MOKE will be shown as the most convenient method to investigate thin film magnetism in Section 6.

3. X-ray magnetic circular dichroism (XMCD)

The other MCD technique that is often utilized is X-ray magnetic circular dichroism (XMCD) [3,22]. XMCD is magnetic circular dichroism in X-ray absorption fine

structure spectroscopy (XAFS). One can refer to recent reviews concerning XMCD [23,24] and, more generally, XAFS [24,25]. As described in Section 2, the larger spin–orbit interaction (and the larger spin polarization) provides the stronger MCD. This implies that when the initial and final one-electron states are, respectively, a core orbital except $L=0$ and a highly spin-polarized orbital, the MCD could be by far stronger than in the case of a valence state excitation. In fact, when we measure for instance the XMCD concerning the dipole-allowed $2p \rightarrow 3d$ transition of Fe thin films, the XMCD intensity amounts to as much as several tens %, which is substantially larger than that of the MOKE intensity of typically $<0.1\%$. This is because of the very strong spin–orbit coupling in the Fe $2p$ core level and of the large spin-polarization in the Fe $3d$ valence band. In the Fe $2p$ orbital, the energy splitting between the $2p_{3/2}$ and $2p_{1/2}$ states is as much as $\sim$13 eV. Figure 6(a) shows the Fe $L_{\mathrm{III,II}}$-edge XMCD of bulk Fe, while Figure 6(b) depicts a schematic view of the basic principle of the XMCD. The selection rule is the same as in the MOKE; the positive and negative helicity light induce the $l_z' = l_z \pm 1$ transitions, respectively.

Another prominent feature in XMCD is the element specificity. Figure 6(c) shows the Fe and Co L-edge XMCD of a GMR-type Fe/Cu/Co/Cu(001) sandwich film. In this Cu thickness, the Fe and Co magnetizations are found to be opposite to each other in the remanent state; Co is normally magnetized following the direction of a magnetic field that has been applied, while Fe shows the magnetization to the opposite direction due to the antiferromagnetic interaction between Fe and Co. Such a phenomenon can easily be detected by means of XMCD owing to its element specificity. Moreover, as shown below, XMCD provides quantitative information on spin and orbital magnetic moments separately through the so-called sum rules [26,27]. Although the total magnetic moment of the system can be accurately determined by means of SQUIDs for instance, the estimation of the orbital magnetic moment is not so easy. The XMCD technique is one of the most suitable methods for this purpose.

3.1. *Theory of XMCD*

Let us here consider the $2p \rightarrow 3d$ transition of $3d$ elements. For simplicity, we will assume that the $3d\alpha$ orbitals are fully occupied, while the $3d\beta$ ones are completely vacant and that all the $3d$ orbitals are degenerate. The transition intensities from the $2p_{3/2,1/2}$ core to the $3d_{2,1,0,-1,-2}$ orbitals are easily evaluated by using hydrogen-like wavefunctions as shown in Figure 7. In the case of $2p_{3/2}$ excitation, the positive and negative helicity light give the total relative transition intensities of $I^+=15$ and $I^-=25$, respectively, leading to a negative XMCD [$\Delta I(L_{\mathrm{III}}) = I^+ - I^- = -10$]. On the other hand, in the $2p_{1/2}$ case, the positive and negative helicity light provide $I^+=15$ and $I^-=5$, respectively, yielding a positive XMCD [$\Delta I(L_{\mathrm{II}}) = I^+ - I^- = +10$]. If all the $3d$ orbitals are degenerate, the sum of the L_{III} and L_{II} XMCD, $\Delta I(L_{\mathrm{III}}) + \Delta I(L_{\mathrm{II}})$, is 0. The Fe $L_{\mathrm{III,II}}$-edge XMCD shown in Figure 6(a) shows a larger area in the L_{III} signal than in the L_{II} one, implying that all the $3d$ orbitals are not equivalent; the $3d\beta$ orbitals are partially occupied and/or are energetically split due to the spin–orbit interaction in the $3d$ levels. This indicates the incomplete cancellation of the orbital magnetic moment. Thole *et al.* [26] and Carra *et al.* [27] have derived the sum rules concerning the orbital m_{orb} and spin m_{spin} magnetic

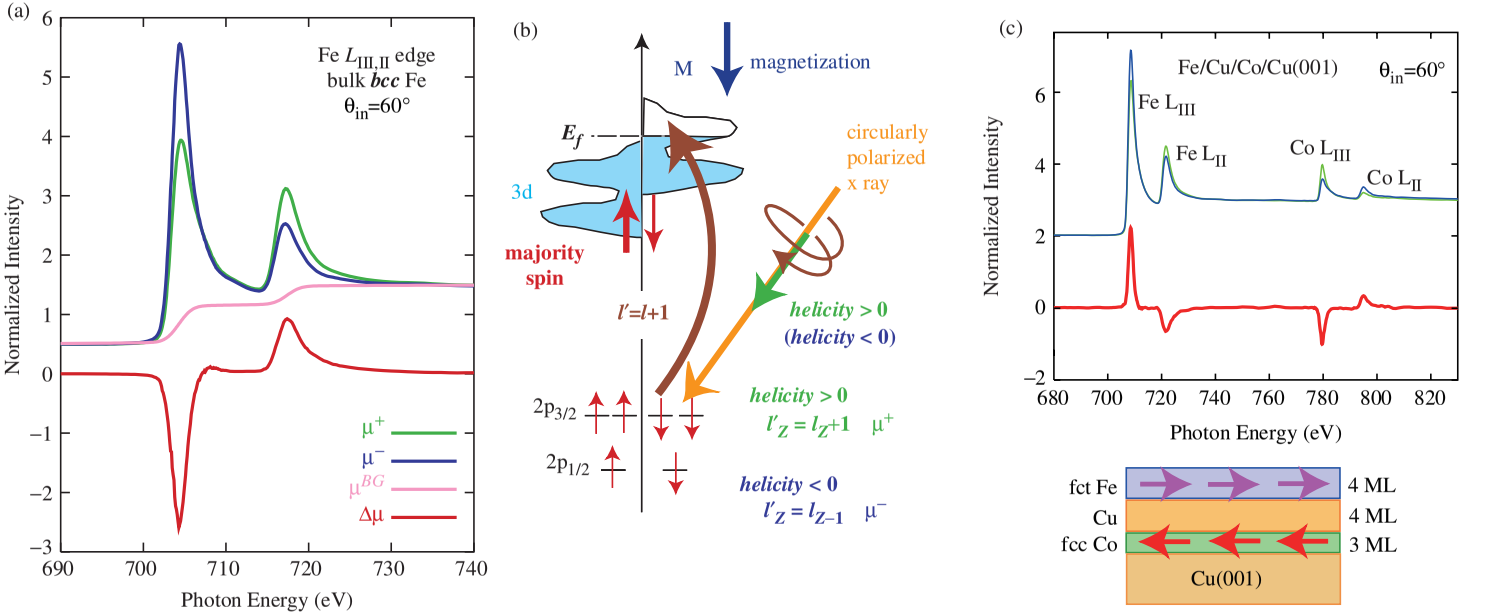

Figure 6. [Colour online] (a) Fe $L_{III,II}$-edge XMCD of bulk Fe. The magnetization is in-plane, while the X-ray incidence polar angle is 60°, and the angle between **M** and **k** is 30°. μ^+ and μ^- are the experimentally obtained parallel and antiparallel spectra. The word 'parallel (antiparallel)' means that the photon helicity and the spin angular momentum of the system are aligned with a parallel (antiparallel) direction. $\Delta\mu$ is the XMCD that is normalized with the polarization factor $|P_c| \cdot (\hat{\mathbf{M}} \cdot \hat{\mathbf{k}}) = 0.70 \times \sqrt{3}/2$. (b) Schematic view of the $2p \rightarrow 3d$ transition in magnetic materials. (c) Fe and Co $L_{III,II}$-edge XMCD of the Fe(4 ML)/Cu(4 ML)/Co(3 ML) trilayer film on Cu(001). Co is normally magnetized following the direction of a magnetic field that has been applied, while Fe shows the magnetization to the opposite direction due to the antiferromagnetic interaction between Fe and Co.

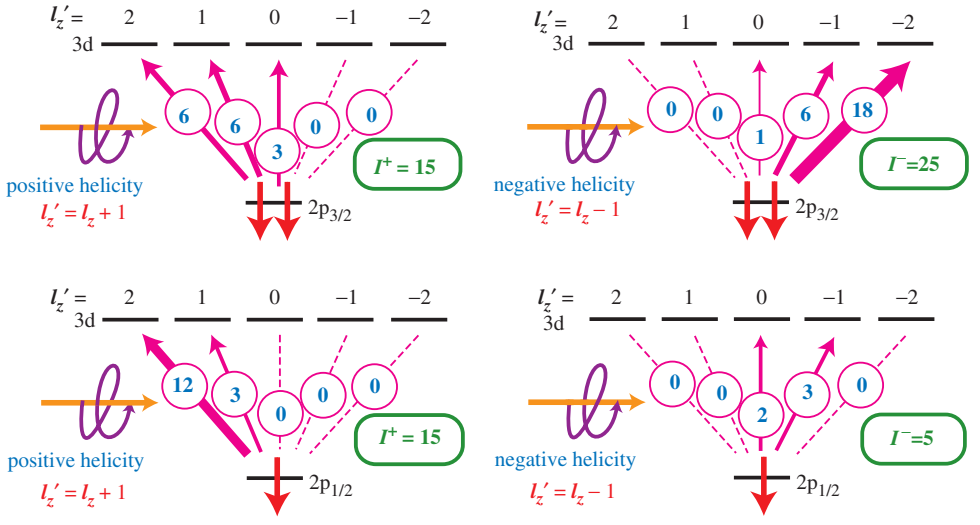

Figure 7. [Colour online] Relative transition probabilities concerning the $2p \rightarrow 3d$ excitation. It is assumed that the $3d\alpha$ orbitals are fully occupied, while the $3d\beta$ ones are completely vacant.

moments as

$$m_{\mathrm{orb}} = \frac{2n_h\mu_B}{3I_{av}} \int_{L_{\mathrm{III}}+L_{\mathrm{II}}} \Delta\mu \, \mathrm{d}E, \tag{20}$$

and

$$m_{\mathrm{spin}}^{\mathrm{eff}} = m_{\mathrm{spin}} + 7m_T = \frac{n_h\mu_B}{3I_{\mathrm{av}}} \left(\int_{L_{\mathrm{III}}} \Delta\mu \, \mathrm{d}E - 2\int_{L_{\mathrm{II}}} \Delta\mu \, \mathrm{d}E \right). \tag{21}$$

Here, $m_{\mathrm{spin}}^{\mathrm{eff}}$ is the effective spin magnetic moment, n_h the d-hole number, μ_B the Bohr magneton, and $\Delta\mu$ the experimentally obtained XMCD spectrum. $m_T = -\langle T \rangle \mu_B/\hbar$ in Equation (21) is the projected magnetic dipole moment along the magnetization direction where

$$\mathbf{T} = \sum_i \left(\mathbf{S}_i - \frac{3\mathbf{r}_i(\mathbf{r}_i \cdot \mathbf{S}_i)}{r_i^2} \right) \tag{22}$$

is the intraatomic magnetic dipole operator. The normalization factor I_{av} corresponds to the experimentally obtained average $L_{\mathrm{III,II}}$ peak area ($2p \rightarrow 3d$ transition intensity) and is given as

$$I_{\mathrm{av}} = \int_{L_{\mathrm{III}}+L_{\mathrm{II}}} \left(\frac{\mu^+ + \mu^-}{2} - \mu^{\mathrm{BG}} \right) \mathrm{d}E, \tag{23}$$

where μ^{BG} is the background absorption spectrum expressed by the two step functions [see Figure 6(a) for μ^+, μ^- and μ^{BG}]. Note that I_{av} is proportional to n_h.

In Equation (21), it is found that the effective spin magnetic moment $m_{\text{spin}}^{\text{eff}}$ can be obtained experimentally, while the determination of the spin magnetic moment m_{spin} requires the subtraction of the magnetic dipole term m_T. Since the magnetic dipole term m_T is not so huge, only the effective spin magnetic moments $m_{\text{spin}}^{\text{eff}}$ have been given in many publications. It is, however, inconvenient when one wants to discuss the magnetization quantitatively. In order to give the absolute number of the spin magnetic moments m_{spin}, Stöhr and König [28] proposed important formulas in the angular dependent XMCD measurement:

$$m_{\text{orb}}(\theta_M, \phi_M) = m_{\text{orb}}^x \sin^2\theta_M \cos^2\phi_M + m_{\text{orb}}^y \sin^2\theta_M \sin^2\phi_M + m_{\text{orb}}^z \cos^2\theta_M \tag{24}$$

$$m_T(\theta_M, \phi_M) = m_T^x \sin^2\theta_M \cos^2\phi_M + m_T^y \sin^2\theta_M \sin^2\phi_M + m_T^z \cos^2\theta_M, \tag{25}$$

$$m_T^x + m_T^y + m_T^z = 0, \tag{26}$$

and

$$m_{\text{spin}}^{\text{eff}}(\theta_M, \phi_M) = m_{\text{spin}} + 7m_T(\theta_M, \phi_M), \tag{21'}$$

where the z axis is the surface normal (not the quantitized axis), and θ_M and ϕ_M are the polar and azimuthal angles of the magnetization **M**. When one measures at least three XMCD spectra at different magnetization angles, the equations can be solved to yield all the quantities m_{orb}^x, m_{orb}^y, m_{orb}^z, m_T^x, m_T^y, m_T^z, and m_{spin}. The important issue for the usage of these equations is that the saturated magnetizations are required for all the magnetization angles, because only at the saturated magnetization is the spin magnetic moment m_{spin} independent of the magnetization angle. Note that m_{orb} and m_T are still angular dependent at the saturated magnetization. This implies that the sample must be magnetized even along the magnetically hard axes. Although most magnetic thin films can be magnetized along the magnetically easy axis with a small external magnetic field **H**, the saturated magnetization along the hard axis requires at least several tesla of **H**. The determination of the angular dependent magnetic moments thus needs a superconducting magnet. When the x and y axes are equivalent in the system of interest, the azimuthal angle dependence is missing, and one can measure only two XMCD spectra to solve the polar angle dependence.

The important quantitative quantity obtained by XMCD is orbital magnetic moments. It is substantially important to understand the relationship between the orbital magnetic moment and the macroscopic magnetic anisotropy. Qualitatively, when one considers the spin–orbit interaction as $E_{\text{SO}} = \xi \mathbf{L} \cdot \mathbf{S}$ (ξ is the spin–orbit coupling constant), larger orbital magnetic moments may provide more stable states. Assuming the validity of the Hund rule that the orbital angular momentum is parallel (antiparallel) to the spin angular momentum in the more (less) than half 3*d* elements, one can understand that the magnetization direction with the largest orbital angular momentum corresponds to the magnetic easy axis through the spin–orbit interaction. Note here that the spin–spin exchange interaction $E_{\text{EX}} = J_{ij}\mathbf{S}_i \cdot \mathbf{S}_j$ (J_{ij} is the exchange coupling constant between atoms i and j) is isotropic due to the scalar product between two spin angular momenta, though the exchange interaction is much larger than the spin–orbit interaction. Bruno [29] presented a quantitative understanding of the relation by means of second-order perturbation theory in itinerant

ferromagnets and found that the magnetic anisotropy energy is proportional to the expectation value of the orbital magnetic moment. Moreover, van der Laan [30] reported additional terms that are related to the spin-subband orbital moment and to the magnetic dipole operator due to the anisotropy of the field of the spin. The difference in the magnetic anisotropy energy ΔE_a is consequently given as

$$\Delta E_a \cong -\frac{1}{4}\xi\hat{\mathbf{S}}\cdot\left[\left\langle\mathbf{L}^{\downarrow}\right\rangle-\left\langle\mathbf{L}^{\uparrow}\right\rangle\right]+\frac{\xi^2}{\Delta E_{\mathrm{EX}}}\left[\frac{21}{2}\hat{\mathbf{S}}\cdot\langle\mathbf{T}\rangle+2\left\langle(L_zS_z)^2\right\rangle\right], \tag{27}$$

where $\hat{\mathbf{S}}$ the unit vector along the spin angular momentum, $\langle\mathbf{L}^{\uparrow(\downarrow)}\rangle$ the expectation value of the orbital angular momentum of the spin up (down) band, and ΔE_{EX} the exchange splitting. The first term was obtained by Bruno [29], while the latter term introduced by van der Laan [30] accounts for the spin-flip excitations between the majority and minority spin bands. It is thus recognized that the microscopic orbital magnetic moment obtained by the XMCD directly provides information on the macroscopic magnetic anisotropy energy.

3.2. *Experimental setup of XMCD*

For the measurements of XMCD, a superconducting magnet is strongly desired. Koide *et al*. [31] pioneeringly developed a UHV compatible XMCD system with a superconducting magnet. There are several experimental and theoretical advantages in measurements under a high magnetic field. Theoretically, as discussed in the above subsection, the determination of the spin magnetic moment and the angular dependent orbital magnetic moments requires a magnetic field high enough to saturate the magnetization even along the hard axes. Since the magnetic anisotropy is one of the most important issues in XMCD studies, the use of a superconducting magnet is thus highly recommended. From the experimental point of view, a lower temperature of the sample is more easily achieved since the sample is almost completely surrounded by the liquid helium reservoirs for the superconducting magnets. The pressure around the sample should also be excellent due to the presence of the liquid helium reservoirs, and a baking procedure for the magnet is not always required. Moreover, since the XMCD spectra can be recorded only by measuring the drain sample current, we do not have to worry about the influence of the high magnetic field to the electronic equipments such as microchannel plates. When the magnetic field is sufficiently high, the electron recoiling to the sample due to the Lorentz force can be neglected to yield a larger drain current than in the low magnetic field.

Figure 8 shows an example of the XMCD measurement system [32] with a superconducting magnet and a liquid helium cryostat installed at Beamline 4B [33] in UVSOR-II of the Institute for Molecular Science (IMS), Japan. The system consists of two separated UHV chambers for the XMCD measurement and the sample preparation. The sample preparation chamber is equipped with metal evaporators, RHEED (reflection high-energy electron diffraction) or LEED/AES (low energy electron diffraction and Auger electron spectroscopy) optics, an ion gun, a sample heating system, and so forth. The measurement chamber was constructed by JANIS Research Company, Inc., MA, USA. The system consists of a superconducting magnet and a variable temperature insert. The magnet is a 7 T(horizontal field) split multi-filamentary NbTi superconducting magnet

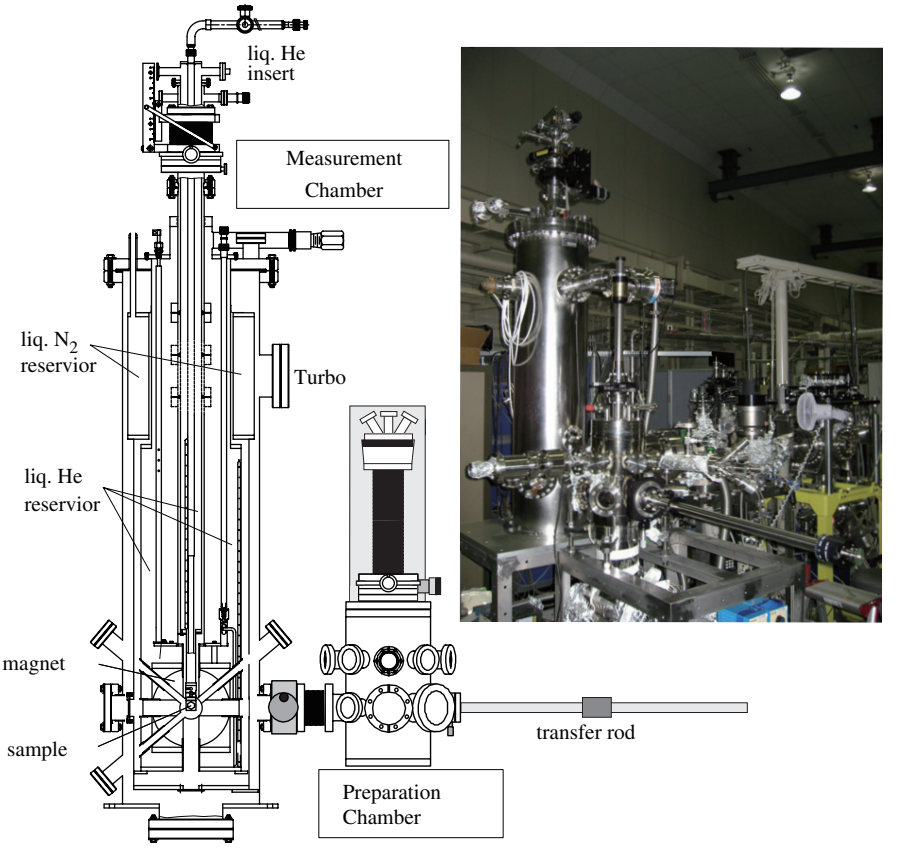

Figure 8. [Colour online] Schematic rear view and photo of the XMCD measurement system. The X-rays come from the back side with a parallel configuration to a magnetic field. The liquid helium reservoir with a 25 L capacity is surrounded by a liquid nitrogen reservoir with a nominal 10 L capacity. From [32].

with field homogeneity of $\pm 0.5\%$ over a 1 cm diameter sphere. The sweep speeds are 1 T/min up to 5 T and 0.25 T/min from 5 to 7 T. A liquid helium reservoir has a 25 L capacity with a minimum of 12 hour static hold time (24 hour hold time without applied magnetic field). The sample cryostat has a built-in heater and two calibrated Cernox thermometers plus a two section high efficiency continuous flow type liquid helium transfer line. This offers the lowest sample temperatures of ~4.8 K during helium accumulated and of ~3.8 K for helium pumped. The sample cryostat can be rotated by 360°, allowing us to measure angular dependent XMCD spectra. A sample holder is a hexagonal shaped Mo with a screw. The base pressure is below 2×10^{-8} Pa at the ionization gauge position and should be much better at the sample position.

The light source should be a soft X-ray synchrotron radiation and a grazing incidence grating monochormator; for the measurements of $L_{\mathrm{III,II}}$-edge XMCD for 3*d* elements, the photon energies required are around 500–1000 eV (512.1 eV for V L_{III}, 932.5 eV for Cu L_{III}, etc.), while for the measurements of $M_{\mathrm{V,IV}}$-edge XMCD for lanthanide elements,

they are in the range of 800–1600 eV (836.0 eV for La M_V, 1527.8 eV for Yb M_V, etc.). Hard X-ray sources are also useful to measure $L_{III,II}$-edge XMCD for 4*d*, 5*d* and lanthanide elements. In order to obtain circular polarization, a helical or polarization variable undulator is the best light source for its high brilliance and high energy resolution due to the low emittance. Although in the soft X-ray region a sophisticated phase retarder has not yet been exploited, rather high speed polarization switching is possible by placing two opposite undulators that provide positive and negative helicity X-rays. A bending magnet beamline is also useful, although the performance is much worse than the undulator. In the bending magnet beamline, the X-rays on the synchrotron orbit plane is linearly polarized, while the upper or lower part from the orbit plane gives elliptically polarized light.

3.3. *Example of XMCD*

Figure 9 is a typical example of the XMCD data recorded at Beamline 4B of UVOSR-II [33]. The circularly polarization factor was estimated as $|P_c| = 0.85 \pm 0.03$. The sample is 0.4 ML Co deposited on Cu(001). It is known that the present sample shows the magnetically easy axis of [110] (within the surface plane) and the hardest axis of [001] (surface normal) [34,35]. Moreover, Co is found to grow in a layer-by-layer fashion, and a 0.4 ML Co film shows mostly single-layer large islands with a small amount of the second layer [35]. Figure 9(c) shows the magnetization curve along the [001] direction. The magnetization was scaled by the area of the Co L_{III} peak around 778 eV. The magnetization is found to increase linearly up to $H = \pm 2.5$ T, while the magnetizations at $H = \pm 5.0$ T are apparently weaker than expected from the extrapolated linear line. The magnetic anisotropy energy E_a of a magnetic thin film under a perpendicular external magnetic field H is phenomenologically expressed in the second-order approximation as

$$E_a = -\frac{1}{2\mu_0} N M_S^2 + K_2 \cos^2 \theta_M - M_S H \cos \theta_M \tag{28}$$

where M_S the saturated magnetization, N the demagnetizing factor ($N = 1$ for infinitely wide film), and K_2 the second-order magnetocrystalline and/or magnetoelastic anisotropic constant. The perpendicular component of magnetization, $M_S \cos\theta_M$, is obtained by minimizing E_a in Equation (28). This yields a linear function up to H_S, while it turns flat above H_S. By fitting the experimentally obtained data points ($|H| < 2.5$ T) with a linear function, H_S is estimated as $\sim$3.4 T. The magnetic fields of ± 5 T are thus confirmed to saturate the magnetization even along the hardest [001] axis.

Figure 9(a) depicts the angular dependent Co $L_{III,II}$-edge circularly polarized X-ray absorption spectra. In the case of the $\theta_{in} = 60^\circ$ spectra (top), the magnetization **M** is still lying flat along [110] with a negligibly small perpendicular component due to a weak magnetic field of $H = \pm 0.1$ T. Thus the angle between **M** and the X-ray propagation direction **k** is 30°. The XMCD spectrum is normalized with a factor of $|P_c| \cos 30^\circ$. On the other hand, the XMCD spectrum (bottom) along the [001] axis was taken at $\theta_{in} = 0^\circ$ (normal X-ray incidence) and $H = \pm 5.0$ T(**H**//[001]). The magnetization saturation is verified. The spectrum is normalized with $|P_c|$. Figure 9(b) shows the XMCD spectra for $\theta_M = 90^\circ$ and 0°. Although the two XMCD spectra are not very different to each other, small dissimilarities can clearly be seen around the $L_{III,II}$-edge peaks. Since the spin

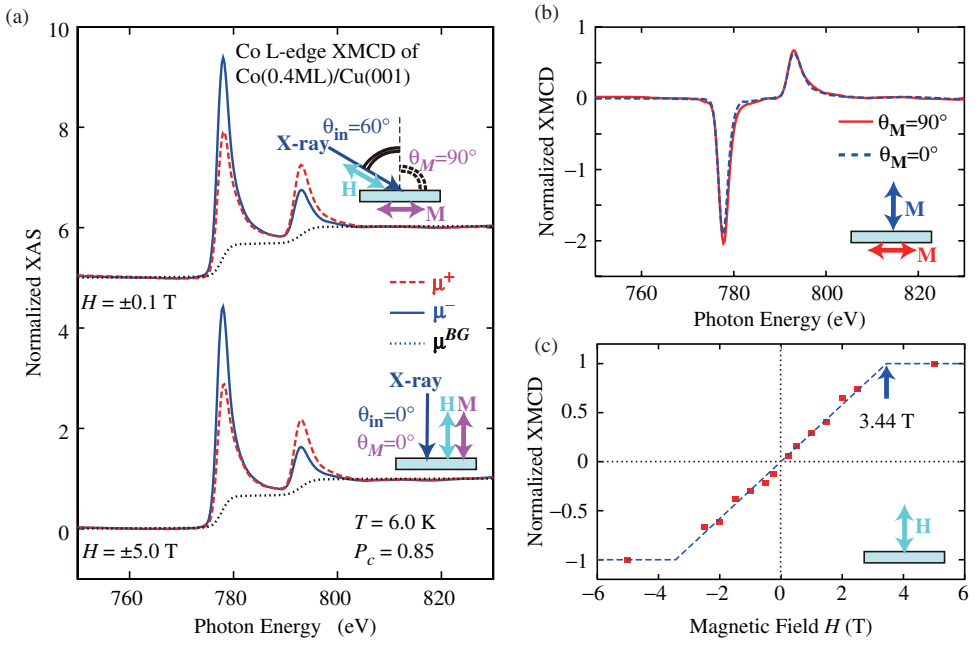

Figure 9. [Colour online] (a) Co $L_{III,II}$-edge circularly polarized X-ray absorption spectra of 0.4 ML Co on Cu(001) at 6.0 K recorded with a total electron yield mode (sample drain current). In the top spectra, magnetization is along the easy axis of [110] within the surface plane ($\theta_M = 90°$), and the X-ray incidence and the external magnetic field (±0.1 T) are directed to $\theta_{in} = 60°$ from the surface normal. In the bottom spectra, the magnetization, the X-ray incidence and the external magnetic field (±5.0 T) are all aligned to the [001] hardest axis: $\theta_M = 0°$ and $\theta_{in} = 0°$. The solid blue and dashed red lines correspond to $\mu^+(\theta_M)$ and $\mu^-(\theta_M)$, while the black dotted lines are the background absorption μ^{BG}. The spectra were self-absorption corrected, although the effect is essentially negligible for the present thickness. (b) Co $L_{III,II}$-edge XMCD spectra of 0.4 ML Co on Cu(001) at 6.0 K for the magnetization parallel ($\theta_M = 90°$) and perpendicular ($\theta_M = 0°$) to the surface. (c) Magnetization curve of 0.4 ML Co on Cu(001) at 6.0 K along the surface normal [001] direction, recorded as a Co L_{III} XMCD intensity. The red points are the experimental data, and the blue dashed line is the fitted result using the second-order approximation of the magnetic anisotropy energy. From [32].

magnetic moment is not angular dependent due to the saturated magnetization in both the directions of the applied magnetic fields, the small difference indicates the contribution of the magnetic dipole term $m_T(\theta_M)$ in Equations (21) and (22) to the anisotropic spectral feature in the present submonolayer film.

In order to give the absolute number of the magnetic moments, the proportional factor of n_h/I_{av} in Equations (20) and (21) is first estimated by using a reference XMCD spectrum of 3.0 ML Co on Cu(001) at 6.5 K, where $n_h = 2.50$ is assumed [36]. As a result in 0.4 ML Co, we obtain the *d*-hole numbers as $n_h(90°) = 2.56 \pm 0.15$ and $n_h(0°) = 2.48 \pm 0.15$, implying that the *d*-hole number is almost angular independent and also similar to that of 3 ML Co. Subsequently, we evaluate the magnetic moments of 0.4 ML Co by using the sum rules as $m_{orb}(90°) = 0.29 \pm 0.05\,\mu_B$, $m_{orb}(0°) = 0.23 \pm 0.05\,\mu_B$, $m_{spin}^{eff}(90°) = 1.86 \pm 0.10\,\mu_B$, and $m_{spin}^{eff}(0°) = 1.65 \pm 0.10\,\mu_B$. We will here assume that the azimuthal (in-plane) magnetic anisotropy of the present film can be neglected. By using Equations (24)–(26)

and (20′), the magnetic dipole terms are given as $m_T^x = m_T^y = m_T^{\parallel} = 0.010 \pm 0.005\,\mu_B$ and $m_T^z = m_T^{\perp} = -0.020 \pm 0.005\,\mu_B$. The spin magnetic moment of $m_{\mathrm{spin}} = 1.79 \pm 0.10\ \mu_B$ is around 12% larger than that of bulk *hcp* Co ($m_{\mathrm{spin}} = 1.55\ \mu_B$), and the orbital magnetic moments of $m_{\mathrm{orb}}^x = m_{\mathrm{orb}}^y = m_{\mathrm{orb}}^{\parallel} = 0.29 \pm 0.05\,\mu_B$ and $m_{\mathrm{orb}}^z = m_{\mathrm{orb}}^{\perp} = 0.23 \pm 0.05\,\mu_B$ are much more significantly greater than the bulk value of $m_{\mathrm{orb}} = 0.15\,\mu_B$. Tischer *et al.* [34] reported $m_{\mathrm{orb}}^{\parallel}/m_{\mathrm{spin}}^{\mathrm{eff}}(90^\circ) \cong 0.10$ around 2 ML Co. The present result gives $m_{\mathrm{orb}}^{\parallel}/m_{\mathrm{spin}}^{\mathrm{eff}}(90^\circ) = 0.16 \pm 0.02$, which is small but meaningfully larger than their result due to a smaller Co thickness in the present case. There have also been reported theoretical estimations for the spin magnetic moment of monolayer Co/Cu(001): $m_{\mathrm{spin}} = 1.71\,\mu_B$ [37], $1.78\,\mu_B$ [38] and $1.85\,\mu_B$ [36]. Although the theoretical estimations are rather scattered depending on the calculation method and the employed lattice constant, 10–20% enhancement of m_{spin} compared to the bulk value are in fairly good agreement with the present finding. Hjortstam *et al.* [36] further evaluated the orbital magnetic moment of $m_{\mathrm{orb}}^{\perp} = 0.261\mu_B$ assuming perpendicular magnetization for calculational simplicity, which is also consistent with the present result.

3.4. *Photoelectron emission microscopy (PEEM) based on XMCD*

Since the XMCD technique usually detects total electron yields, one can immediately recognize that it is applicable to PEEM. Stöhr *et al.* [39] and Schneider *et al.* [40] demonstrated the first domain imaging of magnetic surfaces and thin films by means of XMCD PEEM. When the photon energy is tuned to the energy where the XMCD is most prominently observed (for instance L_{III}-edge peak in 3*d* elements), the magnetic contrast is easily obtained depending on the magnetization direction of each magnetic domain since the magnetic contrast is simply described by $\mathbf{M} \cdot \hat{\mathbf{k}}$. By virtue of the availability of highly brilliant third generation synchrotron radiation X-rays, the XMCD PEEM technique has now matured into a valuable tool to unravel the element specific magnetic microstructure of complex thin film systems. Antiferromagnetic films have also been investigated by applying X-ray magnetic linear dichroism (XMLD). Recently, time-resolved XMCD PEEM has also become an attractive subject by using the well defined time structure of synchrotron radiation [41]. The time resolving power essentially depends on the pulse width of synchrotron radiation and is now in the 10–100 picosecond range. The time resolution is much worse than ultrashort pulsed lasers with a 10–100 femtosecond pulse width. This disadvantage will be overcome soon through the near future operation of X-ray free electron lasers. In this subsection, we will briefly introduce some examples of XMCD PEEM recently published.

3.4.1. *Example of element specific XMCD PEEM*

Kuch *et al.* [42] investigated layer-resolved magnetic domain images of epitaxially grown Co/Cu/Ni trilayers on Cu(001). Figures 10(a) and (b) show respectively the Ni and Co XMCD PEEM images of an as-grown Co(4 ML)/Cu(wedge)/Ni(15 ML)/Cu(001) trilayer. In these trilayers, the Ni layers are magnetized perpendicularly to the film plane, whereas the Co magnetization is in the film plane. The local magnetization direction of Co is indicated by arrows in Figure 10(b) for some domains. The Co domains are mainly magnetized along the [110] (white arrows) and $[\bar{1}\bar{1}0]$ (black) crystallographic directions.

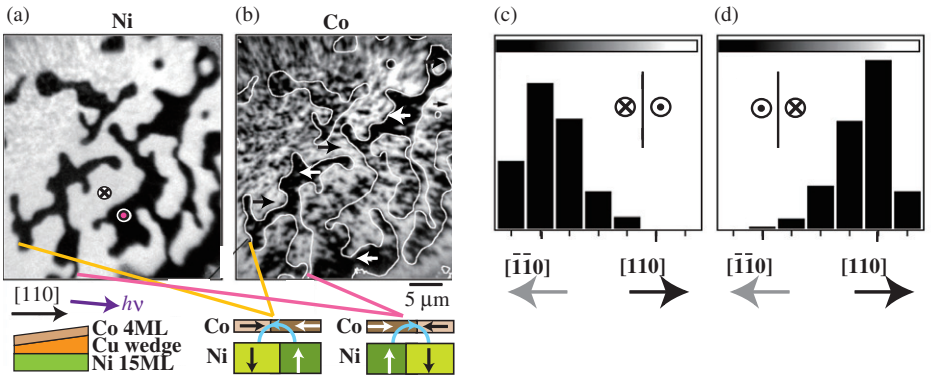

Figure 10. [Colour online] (a), (b) Element resolved domain images of the as-grown Co(4 ML)/Cu wedge/Ni(15 ML)/Cu(001) Trilayer for (a) Ni and (b) Co. The white lines in (b) mark the position of Ni domain walls in (a). (c) Histogram of the Co magnetization contrast above Ni domain wall sections which correspond to the situation shown in the left sketch. (d) The same as in (c) but for Ni domain wall sections corresponding to the right sketch. From [42].

The [110] in-plane directions are the easy axes of Co/Cu(001) [32,33,41]. The artificial white lines in the Co image mark the position of Ni domain walls. They facilitate a discussion of the correlation between the as-grown Ni and Co domain patterns. All the larger black domains in the Co image are related to similarly shaped Ni domains. At about the middle of the image these black domains in Co correspond to black domains in Ni, whereas at the bottom of the image a black domain in Co is located at the position of a white domain in Ni. A closer inspection of the element resolved domain patterns reveals that in regions of correlated domain patterns the domain walls in Co are shifted right or left with respect to the domain walls in Ni. Two such positions are shown by lines at the bottom of Figure 10(b), and the situation at these domain boundaries is illustrated by sketches below the image. The shift of the Co domain walls can be explained by stray fields from the Ni domain walls. Let us first consider the left sketch of Figure 10(b). A domain wall in Ni separates a white (down) domain (black arrow in the sketch) on the left from a black (up) domain (white arrow in the sketch) on the right. This causes a stray field above the Ni film with an in-plane component pointing to the left, as indicated by the light blue rounded arrow in the sketch. The Co layer, at that position, has a white (right) domain (black arrow) on the left hand side, and a black (left) domain (white arrow) on the right hand side. Since the in-plane component of the stray field from the Ni domain wall is pointing to the left, the domain wall in Co is shifted to the left in order to expand the black (left) domain on the expense of the white (right) domain. The other sketch on the right hand side in Figure 10(b) illustrates a spot on the sample where the opposite situation is encountered: here a domain wall is separating a white (right) domain (white arrow) in Co on top of a black (up) domain in Ni (white arrow) on the left hand side from a black (left) domain in Co (black arrow) on top of a white (down) domain in Ni (black arrow) on the right hand side. The stray field above the Ni domain wall is now pointing to the right (light blue rounded arrow). This extends the white (right) domain in Co, and leads to a shift of the Co domain wall to the right.

A statistical analysis of the whole image range is presented as histogram plots in Figures 10(c) and (d). Since the light incidence is from the left, the contrast in the Co image is sensitive to the component of the in-plane magnetization along the image horizontal. The in-plane component of the stray field points perpendicular to the domain wall. Domain wall stray fields along the horizontal direction are consequently caused by Ni domain walls running along the vertical direction of Figure 10(a). The Co contrast found above vertical sections of Ni domain walls was statistically analysed, and its distribution is presented in the form of histogram plots in Figures 10(c) and (d). Figure 10(c) shows the histogram corresponding to the situation of the left sketch, where a Ni domain wall separates a white (down) domain on the left from a black (up) domain on the right. Figure 10(d) shows the histogram corresponding to the situation of the right sketch. It is clearly seen that in the Co layer virtually everywhere above close-to-vertical Ni domain walls the magnetic contrast in Co is either black or white, i.e., pointing to the left or right, depending on the direction of the stray field from the Ni domain wall. This minimizes the Zeeman energy of the Co magnetization in the local stray field of the Ni domain wall.

Consequently, the layer resolved magnetic domain images of the Co/Cu/Ni trilayers prove the importance of the micromagnetic interaction between the two magnetic layers by magnetostatic stray fields from the Ni domain walls. This result demonstrates the importance of domain wall stray field interactions for the interlayer exchange coupling. The apparent strength of the coupling may be influenced by the presence or absence of domain walls, as well as by its type. A detailed knowledge of the magnetization reversal process and the occurrence of domain walls is thus necessary to correctly describe the apparent coupling deduced from magnetization measurements of coupled systems. On the other hand, this opens a way for tailoring the effective coupling strength within the very same system by manipulating the reversal mechanism. An example is the suppression of domain wall creation by applying a transverse field during magnetization switching.

3.4.2. *Time-resolved XMCD PEEM*

Time-resolved XMCD PEEM using synchrotron radiation X-rays with a resolution of $\sim$100 ps has been applied to investigate dynamics of magnetic domain wall motion. Fukumoto *et al*. [44] studied the spin dynamics of magnetic domain wall motion in the FeNi layer of a FeNi/Al_2O_3/Co trilayer by a stroboscopic pump–probe technique. Figure 11 shows images of the nucleation of magnetic domains and their subsequent expansion in the FeNi layer, observed during the bipolar magnetic field pulses of 5.8 mT. The pulse shape is shown in Figure 11(e). The positive and negative parts have the same amplitude (5.8 mT) and length (47 ns). Note that in this experiment, the magnetization of the Co layer was not affected by the field pulses. Figures 11(a)–(d) show the magnetic domain structures in the FeNi layer at different pump–probe delay times, 9, 19, 24, and 29 ns, respectively. The easy axis is parallel to the vertical direction in the images, and the black and white contrasts indicate the magnetization pointing down and up, respectively. The direction of the incoming X-rays with 30 grazing angle to the surface is also indicated in Figure 11(d). Before applying the pulses, the two ferromagnetic layers were magnetically saturated in the same direction. The direction is indicated by the white arrow in Figure 11(d), and corresponds to black contrast. During the pump–probe experiments, the first, negative part of the pulse is in the same direction

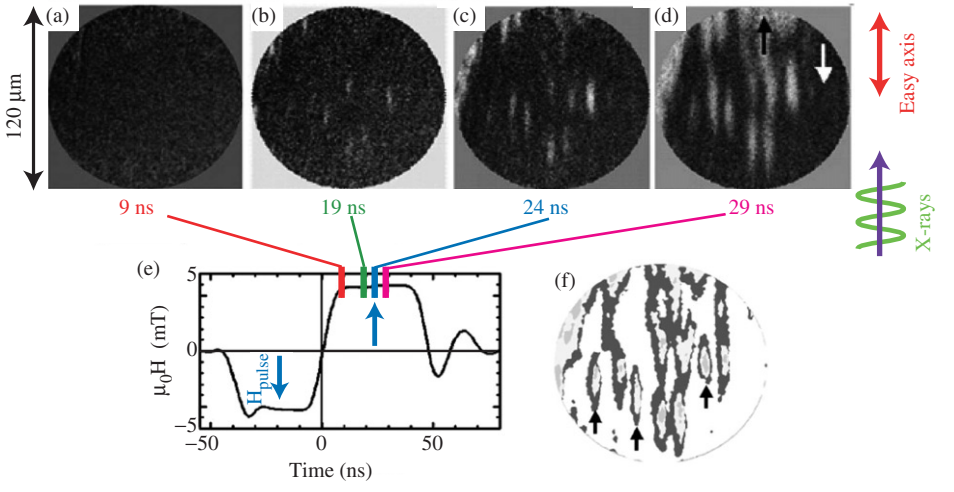

Figure 11. [Colour online] Magnetic domain structures (a)–(d) in the FeNi layer at different delay times after the bipolar magnetic field pulse (e). The pulses were used to reverse the magnetization in part of the FeNi layer. The amplitude of the field pulses was 5.80 mT on the plateaus of both the positive and negative part of the pulses. The photon energy of circularly polarized X-rays was tuned to the Fe L_{III} absorption edge. White domains in (b)–(d) are discretized and superimposed on (f). Different shades of grey in (f) indicate different delay times. Images taken at the Co-L_{III} edge confirmed that no magnetization changes took place in the Co layer. From [44].

as the saturation, and was used to obtain the same starting condition for each pulse. The second, positive part is in the opposite direction [see Figure 11(e)]. The magnetization in the FeNi layer starts to reverse into the white direction during this second part of the pulse. The plateau of the pulse starts at 9 ns, at which time one can see only some small fuzzy white splotches, probably due to magnetic domains that are blocked on surface defects [Figure 11(a)]. Some white domains become visible in Figure 11(b), and, as time goes by, they get larger [Figures 11(c) and (d)]. The areas of white domains in Figures 11(b)–(d) are superimposed on Figure 11(f) with different shades of grey, middle grey, light grey, and dark grey, respectively. The expansion of the domains by propagation of the domain walls is clearly seen. Through the quantitative analysis of the images, it is shown that the reproducible nucleation of domains in the soft layer of a tunnel junction-like trilayer and the subsequent domain growth by domain wall propagation in the viscous regime and up to the Walker limit field is significantly influenced by the energy of magnetic domain walls, leading to an apparent delay of domain expansion. A faster magnetization reversal, which is required for the coming magnetic recording devices, is drastically hindered by this magnetic domain wall energy when magnetic domains are small.

4. Magnetization induced second harmonic generation (MSHG)

Besides the MOKE and XMCD techniques, the other methods based on MCD have been exploited. The magnetization induced second harmonic generation (MSHG) technique

is useful for the investigations of surface and interface magnetization, because SHG is inhibited in the bulk of centrosymmetric crystals. Moreover, in the case of linear MOKE, the signal-to-background ratio is usually very low, while the MSHG gives much larger signals due to the different formalism. In this section, the theory, the experimental method and the application of MSHG are described.

4.1. *Theory of MSHG*

The fundamental theory on MSHG can be found in the textbook [45], and we will review the theory only briefly. In the electric dipole approximation, the polarization vector induced by the light can be written as an expansion in powers of the electric field vector $\mathbf{E}(\omega)$:

$$\mathbf{P}(\omega, 2\omega, \ldots) = \boldsymbol{\chi}^{(1)}\mathbf{E}(\omega) + \boldsymbol{\chi}^{(2)}\mathbf{E}(\omega)\mathbf{E}(\omega) + \cdots. \tag{29}$$

The tensor $\boldsymbol{\chi}^{(1)}$ is the linear optical susceptibility allowed in all media. SHG is described by the second term with the corresponding nonlinear tensor $\boldsymbol{\chi}^{(2)}$ allowed only in noncentrosymmetric media. This can be easily verified by carrying out the inversion operation that changes the sign of every polar vector such as **P** and **E**. Consequently, $\boldsymbol{\chi}^{(2)}$ is allowed at the surface/interface sensitivity of the technique. For crystals with magnetization **M**, the nonlinear second-order optical polarization of a medium $\mathbf{P}^{nl}(2\omega)$ can be given as:

$$\mathbf{P}^{nl}(2\omega) = \boldsymbol{\chi}^{\mathrm{cr}}\mathbf{E}(\omega)\mathbf{E}(\omega) + \boldsymbol{\chi}^{\mathrm{magn}}\mathbf{E}(\omega)\mathbf{E}(\omega)\mathbf{M}, \tag{30}$$

where the first term describes the purely crystallographic contribution, while the second one exists only in the presence of **M** and describes MSHG. Note that **M** is an axial vector, so that the inversion operation does not change its sign and the surface/interface sensitivity also holds for magnetic materials.

For high symmetry systems, each of these tensors consists of a few components only. Moreover, these components do not intermix with each other, that is, the tensor

$$\boldsymbol{\chi}^{(2)} = \boldsymbol{\chi}^{\mathrm{cr}} + \boldsymbol{\chi}^{\mathrm{magn}} \cdot \mathbf{M} \tag{31}$$

can be written as a single third rank tensor, whose components are either even or odd in **M**. Consider a (001) surface of a cubic system as shown in Figure 12(a). The nonlinear tensor $\boldsymbol{\chi}^{(2)}$ is expressed as [46,47]

$$\boldsymbol{\chi}^{(2)} = \begin{pmatrix} \chi_{xxx}(M_y) & \chi_{xyy}(M_y) & \chi_{xzz}(M_y) & \chi_{xzy}(M_z) & \chi^{\mathrm{cr}}_{xzx} & \chi_{xxy}(M_x) \\ \chi_{yxx}(M_x) & \chi_{yyy}(M_x) & \chi_{yzz}(M_x) & \chi^{\mathrm{cr}}_{yzy} & \chi_{yzx}(M_z) & \chi_{yxy}(M_y) \\ \chi^{\mathrm{cr}}_{zxx} & \chi^{\mathrm{cr}}_{zyy} & \chi^{\mathrm{cr}}_{zzz} & \chi_{zzy}(M_z) & \chi_{zzx}(M_y) & \chi_{zxy}(M_z) \end{pmatrix}. \tag{32}$$

Here the magnetization component in parenthesis indicates the $\boldsymbol{\chi}^{(2)}$ element is an odd function of the magnetization component; namely, $\chi_{xxx}(M_y)$ is odd with respect to M_y for instance.

The $\boldsymbol{\chi}^{(2)}$ tensor allows us to understand the behaviour of MSHG qualitatively as a function of magnetization reversal. In the transverse geometry, $\mathbf{M}//y$, when the incidence light is *S*-polarized ($\mathbf{E}_{\mathrm{in}} = \mathbf{E}_y$), one even element χ_{zyy} and one odd element $\chi_{zyy}(M_y)$ will

produce the outgoing wave. Both of them lead to the same *P*-polarization of the output. The total MSHG output can thus be written as [48,49]

$$I^{2\omega}(\pm\mathbf{M}) \propto |E_{in}|^4(\alpha\chi_{zyy} \pm \beta\chi_{xyy}), \tag{33}$$

where α and β denote the corresponding Fresnel coefficients, leading to a change in the MSHG intensity upon a reversal of **M**. On the contrary, in the longitudinal geometry, $\mathbf{M}//x$, the corresponding odd element $\chi_{yyy}(M_x)$ gives rise to an *S*-polarized output. The total output polarization will thus be a vector sum of the two orthogonal vectors, one of them being reversed upon a reversal of **M**. In both cases, the relative effects can be quite large, as the odd and even elements are of similar size. This is in strong contrast to the linear magneto-optical effects, where the odd components are generally much smaller than the even ones.

4.2. *Experimental setup of MSHG*

Figure 12(b) shows a typical MSHG setup in a UHV condition [50,51]. Since the MSHG intensity is proportional to the square of the instantaneous density of the incident light, the light source should be an ultrashort pulsed laser. For this purpose, a femtosecond Ti : sapphire oscillator laser (~800 nm) may be the best candidate. In Figure 12(b), a 80 MHz pulsed laser is directly used. Insertion of a regenerative amplifier significantly improves the intensity of the incident light, although care should be taken of sample damage and/or heating. A filter in the incident beam is used to cut off the second-order harmonics generated in the polarizer and a wave plate, if any. Generated second-order harmonics pass the polarizer and filter before entering the detector. The filter cuts off the fundamental light. When the background light cannot be neglected, one can use a lock-in detection by employing a chopper. A photon counting method is also sometimes useful to improve the signal-to-noise ratio. In the MSHG experiments, the measurement of polarization dependence is also interesting because of different selection rules that provide different information.

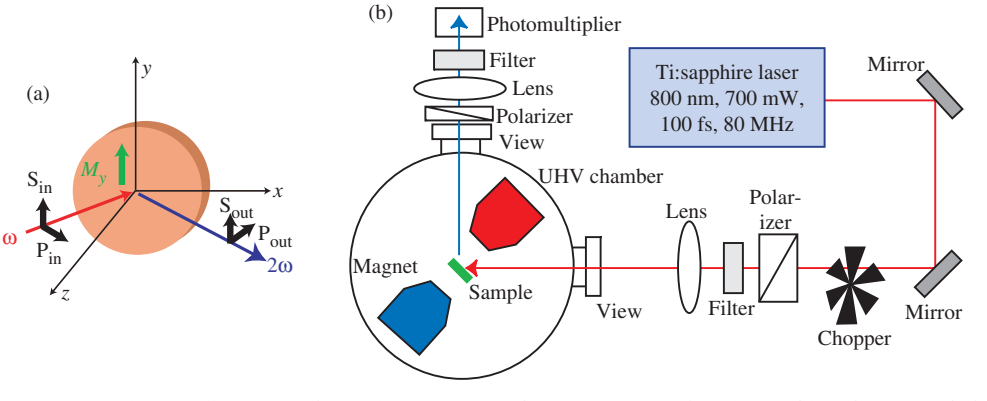

Figure 12. [Colour online] (a) Schematic geometry of MSHG. *xz* is the plane of incidence, and the input light is either $P(E_x, E_z)$ or $S(E_y)$ polarized. The magnetization **M** is directed along the *y* (transverse) or *x* (longitudinal) axis. (b) Experimental setup for the MSHG measurements. See text for details.

For convenience of the experiments, the total MSHG response from a magnetic material should be better to simplify as

$$P(2\omega) = \left(\chi_{\text{eff}}^{\text{even}} \pm \chi_{\text{eff}}^{\text{odd}}(\pm\mathbf{M})\right) E_{\omega}^{2}, \tag{34}$$

where $\chi_{\text{eff}}^{\text{even}}$ and $\chi_{\text{eff}}^{\text{odd}}$ are effective tensor components that are even and odd with respect to **M** and describe the crystallographic and magnetic contributions to the total response, respectively. For the transverse geometry, which is expected to be the most efficient, one can define a MCD asymmetry A as

$$A = \frac{I^{2\omega}(+M) - I^{2\omega}(-M)}{I^{2\omega}(+M) + I^{2\omega}(-M)} = \frac{2|\chi_{\text{eff}}^{\text{even}}||\chi_{\text{eff}}^{\text{odd}}|}{|\chi_{\text{eff}}^{\text{even}}|^2 + |\chi_{\text{eff}}^{\text{odd}}|^2} \cos\Delta\Phi, \tag{35}$$

where $\Delta\Phi$ is the phase difference between the two contributions. When $\Delta\Phi = \pi/2$, the third term is zero and no MSHG signal is observed by changing the magnetization direction. Since A is normalized with the total SHG intensity, it does not depend on the intensity or shape of the fundamental light, nor on the properties of optical elements such as filters.

4.3. *Examples of MSHG*

Figure 13 gives typical examples of the MSHG. Figure 13(a) shows the MSHG of Co(7 ML)/Cu(001), together with the MOKE result. Since the MSHG geometry is longitudinal (**M**//x) and the $\mathbf{E}_{\text{in}}$ is P-polarized, two odd elements χ_{yxx} and χ_{yzz} shows the MSHG. As is apparent in the figure, the MSHG rotation angle is more than one order of magnitude larger than that of MOKE, implying high sensitivity of MSHG.

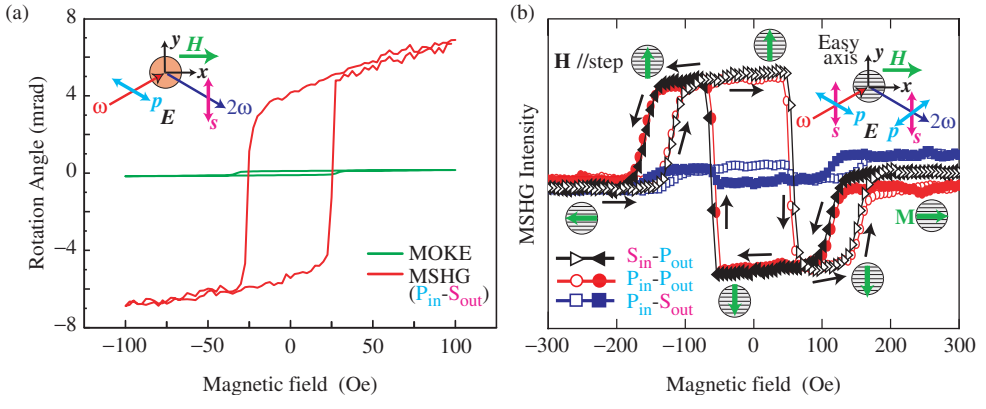

Figure 13. [Colour online] (a) Magnetization curves of Co(7 ML)/Cu(001) recorded with MOKE (green) and MSHG (red). The rotation angle of MSHG is more than one order of magnitude larger than that of MOKE. (b) MSHG magnetization curves of Ag/Co(5 ML)/Cu(1 1 17). The magnetically easy axis is perpendicular to the step (y axis), while the magnetic field applied H is parallel to the parallel step. Polarization dependence is also given; for instance S_{in}–P_{out} denotes the S-polarized incident fundamental light and the P-polarized generated second harmonics. Also shown are the scan directions of the magnetic field, and the schematic magnetization direction during the technical magnetization. From [52].

Figure 13(b) exhibits the polarization dependent MSHG of Ag-coated Co on Cu(1 1 17) [52]. The sample is discussed in detail in Section 6.5; the Cu(1 1 17) substrate crystal provides the step surface with a Cu(001) terrace, and the magnetically easy axis is perpendicular to the step direction (y axis). Although the measurement geometry is longitudinal ($\mathbf{H}//x$) along the hard axis, the transverse magnetization ($\mathbf{M}//y$) can also be observed in the low magnetic field region. The remaining non-zero elements are χ^{cr}_{zyy} and $\chi_{xyy}(M_y)$ for $S_{in}-P_{out}$, $\chi_{yxx}(M_y)$ and $\chi_{yzz}(M_y)$ for $P_{in}-S_{out}$, and $\chi^{cr}_{xzx}, \chi^{cr}_{zxx}$, $\chi_{zzx}(M_y)$ and $\chi_{xxx}(M_y)$ for $P_{in}-P_{out}$. Therefore, the longitudinal contribution ($\mathbf{M}//x$) is observed in the $S_{in}-P_{out}$ case, while the transverse contribution ($\mathbf{M}//y$) can be seen in the $P_{in}-S_{out}$ and $P_{in}-P_{out}$ cases. As seen in Figure 13(b), the transverse $P_{in}-S_{out}$ and $P_{in}-P_{out}$ curves are actually identical to each other and are much more intense than the longitudinal $S_{in}-P_{out}$ one. One can recognize the magnetization procedure of the present sample as depicted in Figure 13(b). When we start to apply $\mathbf{H}$ from $H=+300$ Oe, the magnetization $\mathbf{M}$ is completely aligned to $\mathbf{H}$ ($+x$, hard axis). With decreasing H, $\mathbf{M}$ turns downwards ($-y$, easy axis) at $+100$ Oe. At ~ -100 Oe, $\mathbf{M}$ is once reversed to the upward direction ($+y$, easy axis), and at ~ -200 Oe $\mathbf{M}$ is resultantly aligned to the left ($-x$, hard axis). Although the MSHG technique is usually emphasized to be surface sensitive, it also allows us to extract the transverse Kerr like effect without changing the experimental configuration, which is useful to investigate technical magnetization processes of ultrathin films.

5. Threshold photoemission MCD

The MOKE from ultrathin films in UV–visible light usually exhibits Kerr rotation and ellipticity only of 10^{-2}–10^{-6} radians because of weak spin–orbit interaction in the valence shells. In valence band photoemission, nevertheless, extensive sophisticated work has been performed using circularly polarized synchrotron radiation and an angle-resolved spectrometer [53–55]. It has been shown that the photoemission MCD asymmetry is high enough to be measured (sometimes ~30% particularly near the Fermi level). Normal photoemission is however essentially important for large MCD asymmetry, and angle integrated experiments was believed to degrade the asymmetry, although they are crucial to PEEM measurements. As described in Section 1, Marx *et al*. [6] have successfully observed for the first time UV MLD PEEM with a Hg lamp. They found, however, only 0.19% MCD asymmetry on a very thick Fe film of 100 nm. On the contrary, Nakagawa and Yokoyama [4] observed more than 10% MCD in ultrathin (~10 ML) Ni films when the photon energy was tuned to the work function threshold, and actually they succeeded in the observation of beautiful UV MCD PEEM images [5]. The discovery of the substantial enhancement of the photoemission MCD intensity has opened a new way to femtosecond MCD PEEM using ultrashort pulsed lasers. Since the threshold photoemission MCD method exhibits some advantages compared to MOKE besides applicability to PEEM, the method itself should be worth reviewing here. The advantages may be ascribed to (1) no requirements of the reflected light and (2) the applicability to MLD measurements. This is thus useful when the sample surface is not a mirror face. Moreover, measurements in a high magnetic field should be easier than MOKE since in the MOKE measurement a high magnetic field leads to non-negligible magneto-optical contribution from viewing ports or other optical elements.

5.1. *Experimental setup of threshold photoemission MCD*

Figure 14(a) schematically shows an experimental setup for threshold photoemission MCD/MLD measurements. The sample is in an UHV chamber equipped with an UHV-compatible electromagnet (max. 3000 Oe). Visible and UV lasers are introduced into the chamber through a quartz window. The incident light is circularly (linearly) polarized using a quarter-wave (half-wave) plate with a Glan–Tyler polarizer. For the modulation technique, we use a photoelastic modulator [11,12], which works at the frequency of 50 kHz for the wavelength range of 200–1000 nm. Since the photon energy must be larger than the work function, one should employ in principle deep UV lasers (<220 nm) to measure photoemission MCD. Moreover, when one wants to optimize the MCD asymmetry, a tunable deep UV laser is required. An alternative way may be continuous variation of the work function of the system. This can be achieved by deposition of alkali metals on ultrathin films, if one permits the modification of the system of interest. Here, a HeCd laser (325 nm, CW) and laser diodes (635 and 405 nm, CW) were used as exciting sources, and the installation of a tunable deep UV laser is in progress. The sample drain current is measured as a total photoelectric yield. To avoid distortion of the electric current measurements due to an external magnetic field, an anode with an applied voltage of 1–2 kV is placed in front of the sample. The sample drain current is converted to the voltage by a fast current amplifier, which is subsequently scaled with a DC multimeter or a lock-in amplifier (first and second harmonics). In the same experimental setup using the photoelastic modulator, MOKE can be examined simultaneously. In case of large MCD asymmetry (for instance more than a few per cent), the magnetic hysteresis curves can be obtained without using the photoelastic modulator, and the DC current measurements using a quarter-wave plate is sufficient. The photoelastic modulator is placed with its axis 45° off the electric field vector **E** of the incident light. The magnetic field **H** can be applied horizontally up to 3000 Oe. In the polar and longitudinal MOKE setup, the angle between the light incidence and the surface normal of the sample is 45°.

As a deep UV light source, a free electron laser (FEL) from Beamline 5U of UVSOR-II at the Institute for Molecular Science [54] was used in this experiment. The FEL pulses are extracted through the backward mirror and transported to the measurement chamber through a multilayer mirror. The wavelength varies from 215 to 250 nm and the average FEL power is a few hundred mW in the present setup. Since the FEL is generated from a helical undulator, the light is inherently circularly polarized. The threshold photoemission MCD measurement is performed without wave plates.

The MCD and MLD asymmetries are respectively defined as

$$A^{\mathrm{MCD}} = \frac{I^+ - I^-}{I^+ + I^-} \quad \text{and} \quad A^{\mathrm{MLD}} = \frac{I(\mathbf{M}//\mathbf{E}) - I(\mathbf{M}\perp\mathbf{E})}{I(\mathbf{M}//\mathbf{E}) + I(\mathbf{M}\perp\mathbf{E})}, \tag{36}$$

where I^+ (I^-) is the drain current with positive (negative) helicity light and $I(\mathbf{M}//\mathbf{E})$ ($I(\mathbf{M}\perp\mathbf{E})$) is that for MLD with $\mathbf{M}//\mathbf{E}$ ($\mathbf{M}\perp\mathbf{E}$). With the use of the photoelastic modulator, we obtain the MCD asymmetry [11,12] as the ratio between the first harmonic and DC signals, $A^{\mathrm{MCD}} = I(\omega)/I(\mathrm{DC})$ with the retardation of the photoelastic modulator set at 0.250, and MLD asymmetry as the ratio between the second harmonic and DC signals, $A^{\mathrm{MLD}} = I(2\omega)/I(\mathrm{DC})$ with the retardation of the photoelastic modulator set at 0.500.

Thin films of Fe, Ni, and Co were deposited onto clean Cu(001) surfaces. To change the sample work function, Cs was deposited from commercial dispensers

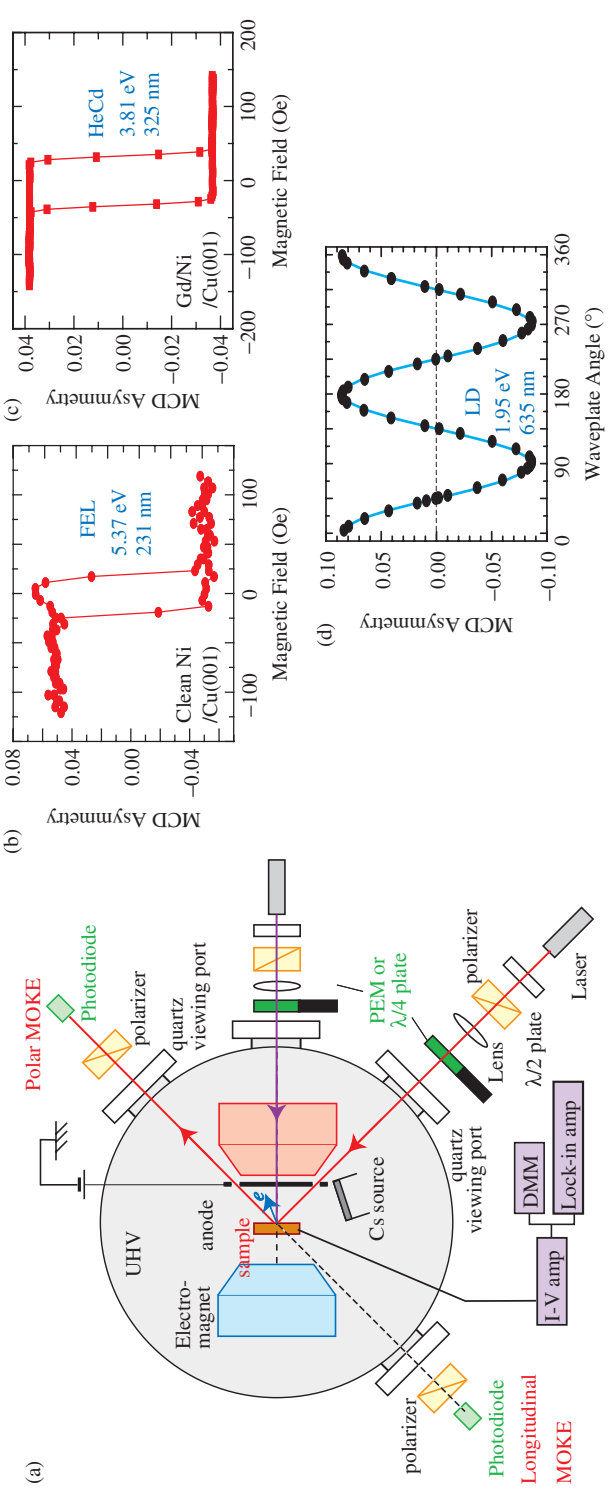

Figure 14. [Colour online] (a) Experimental setup (top view) for the photoemission MCD/MLD measurements. Using a photoelastic modulator, the MOKE can be taken at the same time. In the figure a polar configuration is shown, but rotating the sample allows a longitudinal configuration and angle dependent measurements. (b) Magnetization curve of clean Ni/Cu(001) by using a free electron laser ($h\nu = 5.37$ eV). (c) Magnetization curve of Gd/Ni/Cu(001) by using a HeCd laser ($h\nu = 3.81$ eV). (d) MCD asymmetry as a function of the azimuthal angle of the quarter-wave plate. The curve is perfectly fitted with the cosine function, implying that the observed signal is definitely MCD. From refs. [4,5].

at a rate of 0.001–0.01 ML/min. In the present experimental setup, the Cs or other metal deposition can be performed *in situ* during the MOKE and threshold photoemission MCD/MLD measurements. Instead of Cs, Gd was also deposited on Ni/Cu(001) from a Mo crucible heated by electron bombardment. The work function of Gd/Ni/Cu(001) is sufficiently low to obtain a photoelectric current using the HeCd laser.

5.2. *Enhancement of photoemission MCD near the work function threshold*

Figure 14(b) shows a magnetization curve of perpendicularly magnetized ~10 ML Ni/Cu(001) [57] taken with the threshold photoemission MCD using the FEL of 5.37 eV (231 nm), which is close to the work function of the sample. The threshold photoemission MCD curve shows as much as 5% MCD asymmetry, which is far larger than the MOKE asymmetry of <0.1%. As described above, in-laboratory experiments did not allow us to use a laser whose energy is high enough to excite photoelectrons from Ni. Therefore, we have modified the surface by depositing materials with a lower work function. Figure 14(c) shows the magnetization curve of perpendicularly magnetized Gd(2 ML)/Ni(12 ML)/Cu(001) recorded by the threshold photoemission MCD. The HeCd laser of 3.81 eV (325 nm) was employed and the light incident angle θ_{in} is 45°. Note that the photon energy of 3.81 eV is high enough to emit photoelectrons when depositing Gd on Ni/Cu(001) without Cs adsorption. The threshold photoemission MCD asymmetry obtained is again as much as 4% with a sufficiently high signal-to-noise ratio. Figure 14(d) shows the photoemission MCD asymmetry as a function of the azimuthal angle of the quarter-wave plate. The angles of 0° and 90° correspond to the circular polarization with negative and positive helicities, respectively, while the angle of 45° to the linear polarization. The MCD asymmetry is perfectly fitted with the cosine function. The cosine dependence verifies that the angular moment delivered by the photon polarization gives rise to the present MCD.

Figure 15(a) shows results of the MCD asymmetry using the photon energies of 3.81 and 1.95 eV in successive experiments on the same sample. The work function can be changed by Cs adsorption in the range of 5.4–1.5 eV. The horizontal scale represents the maximum kinetic energy of the photoelectrons, namely the photon energy $h\nu$ subtracted by the work function. The drain currents, I^+ and I^- in Equation (36), at the energy of $h\nu - \Phi$, correspond to the integrated photoemission yield in the energy range between $E_F + \Phi - h\nu$ and E_F (E_F the Fermi level). The most striking result in Figure 15(a) is that the obtained MCD asymmetry is as much as 10–12% near the photoemission threshold and is suppressed quickly as the energy $h\nu - \Phi$ becomes larger. The abrupt reduction of the MCD asymmetry against Cs deposition does not stem from the deterioration of the surface due to Cs. This is evidenced by the two different experiments using the 1.95 and 3.81 eV lasers. In spite of the fact that for the 1.95 and 3.81 eV laser experiments the Cs amounts were about one order of magnitude different around the threshold energy (~0.15 and ~0.03 ML, respectively), the MCD asymmetry curves are almost identical to each other. For further confirmation, Figure 15(b) shows the calculated results for bulk Ni by using the first-principles band structure calculation code WIEN2k [58–60], which also exhibits enhanced MCD asymmetries near the work function threshold and are not significantly dependent on the photon energies.

Apart from the reflection of light, the MCD asymmetry basically depends on both the spin–orbit coupling and the spin polarization (exchange interaction). This is also the case

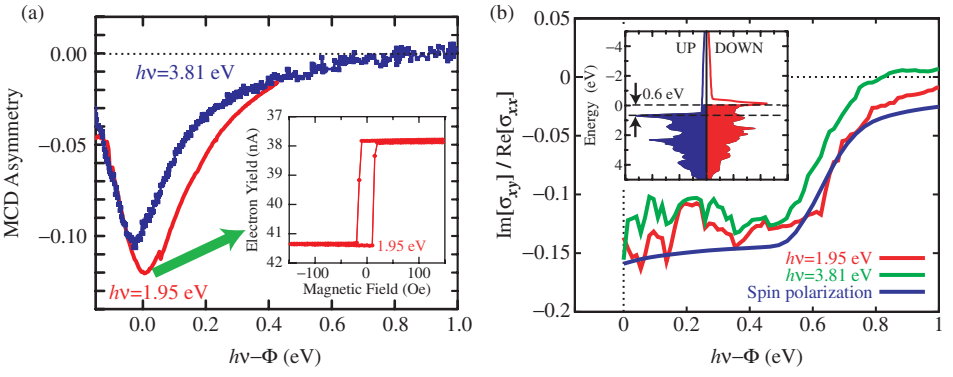

Figure 15. [Colour online] (a) Energy dependence of the photoemission MCD asymmetry from Cs/Ni/Cu(001). The blue and red lines denote the photon energies of 3.81 and 1.95 eV, respectively. Large negative MCD was observed at the work function threshold in both cases. The inset shows the magnetization curve of Cs-coated Ni(12 ML)/Cu(001) using the laser diode ($h\nu = 1.95$ eV and $h\nu - \Phi \cong 0$). (b) Calculated photoemission MCD from bulk Ni by using the WIEN2k code. The blue line corresponds to the spin polarization. The energy dependence of the calculated MCD asymmetry is qualitatively in good agreement with the experimental ones. The inset is the spin-dependent density of states. From [4].

for the Kerr rotation and ellipticity [61]. The MCD asymmetry is basically proportional to the magnitude of the spin–orbit coupling. Thus the observed large MCD asymmetries are partly ascribed to large orbital magnetic moments in ultrathin films. The present calculation, however, indicates that the abrupt drop of the calculated MCD asymmetry in Figure 14(b) is associated with the change of the spin polarization in the integrated photoemission intensity and that the spin–orbit coupling does not change drastically in this narrow energy range around the threshold. On the other hand, near the threshold the photoelectrons along the surface normal [ΓX direction in Ni(001)] are mainly probed, and it is experimentally known that the initial states for the threshold photoemission dominantly correspond to the minority band near the X point [55,62,63]. With increasing the energy $h\nu - \Phi$, the transition in the majority band should begin to take place, leading to a reduction of the spin polarization. Accordingly, the suppression and the sign reversal of the MCD asymmetry observed experimentally in the present work can be attributed mainly to the spin polarization.

5.3. *Photoemission MCD and MLD from in-plane magnetized Co/Cu(001)*

The perpendicularly magnetized Ni/Cu(001) film gives astonishingly large photoemission MCD near the work function threshold. The in-plane magnetized film was investigated. Figure 16(b) shows the magnetization curve of in-plane magnetized Cs/Co(15 ML)/Cu(001) recorded with the threshold photoemission MCD. The MCD asymmetry is found to be ~0.4%, which is far smaller than the Ni/Cu(001) case, although the present Co film has 4–5 times larger magnetization than the previous Ni film. The magnitude of the longitudinal MOKE given in Figure 16(a) is 0.6 mrad, which amounts to 0.06% asymmetry. Although the absolute value of the MCD asymmetry is quite small, the enhancement of the threshold photoemission is again verified. The other examples

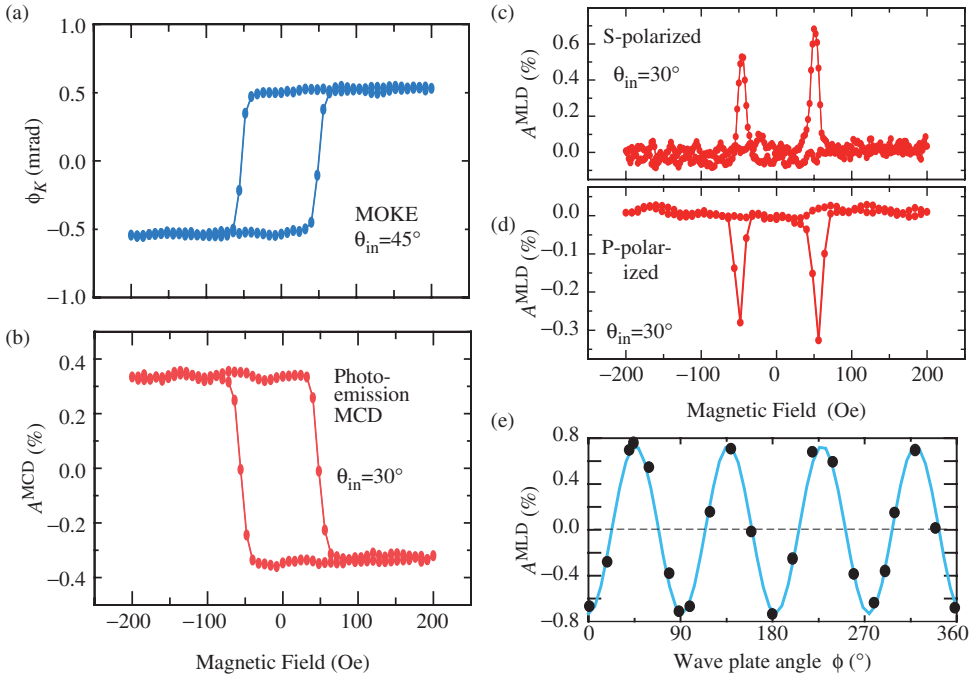

Figure 16. [Colour online] (a)–(d) Magnetization curves of Cs/Co(15 ML)/Cu(001) at 90 K, taken with (a) the threshold photoemission MCD, (b) the longitudinal MOKE, (c), (d) the threshold photoemission MLD using (c) *P*- and (d) *S*-polarized light. (e) The threshold photoemission MLD asymmetry (filled circles) of Cs/Co(15 ML)/Cu(001) as a function of the azimuthal angle of the half-wave plate. The light incident angle θ_{in} is 0° (normal incidence). The results are fitted with a cosine curve of the 4ϕ phase (dashed line). All the data of (a)–(e) are taken with the laser diode (635 nm). From [5].

such as in-plane magnetized Ni/Cu(001), *bcc* Fe/Cu(001) and perpendicularly magnetized Fe/Cu(001) were investigated, and it can be consequently remarked that in general the in-plane magnetized films show much smaller MCD asymmetries than the perpendicularly magnetized ones, although the substantial enhancement of the threshold photoemission MCD compared to the usual photoemission MCD away from the threshold as well as the MOKE results were similarly observed in both cases [4]. The reason for weak MCD asymmetries in the in-plane magnetized films is the same as in the longitudinal MOKE case, which shows much smaller signals than the polar MOKE. Namely, the presence of the reflected light leads to the cancellation of the MCD in the longitudinal configuration.

Figures 16(c) and (d) show the magnetization curves of Cs/Co(15 ML)/Cu(001) recorded with the threshold photoemission MLD, where the light incident angle θ_{in} is 30°. In the *S*- and *P*-polarized threshold photoemission MLD curves, there can be found spikes at the coercive field, which coincide with the MCD and MOKE magnetization curves that show the shape of a parallelogram with coercive field of ~50 Oe. The MLD feature can be understood in the following manner. Consider a horizontal plane that contains the magnetic field **H** and the light propagation vector **k**. When the magnetization **M** is in the

horizontal plane, there should be no MLD in the magnetization reversal operation [55]. Thus, the photocurrent for the saturated magnetization should be the same on both positive and negative sides ($|\mathbf{H}| > 60$ Oe). No magnetic hysteresis loop can thus be obtained with the MLD setup. The observed spikes are attributed to the magnetization component perpendicular to the magnetic field within the surface plane. Since the present films exhibit fourfold symmetry, the vertical axis within the film surface also corresponds to the magnetic easy axis. The vertical magnetization should provide a different photocurrent from the horizontal magnetization and is actually observed as spikes in Figures 16(c) and (d). Figure 16(e) shows the threshold photoemission MLD asymmetry of Cs/Co(15 ML)/Cu(001) using the laser diode (635 nm) as a function of the azimuthal angle ϕ of the half-wave plate. The light incident angle θ_{in} is 0° (normal incidence), and the magnetic field is fixed at 200 Oe along the horizontal axis within the sample surface. At the angles giving minima and maxima in Figure 16(e), the dichroic signals correspond to the difference of the photocurrents between the $\mathbf{M}//\mathbf{E}$ and $\mathbf{M}\perp\mathbf{E}$ cases. The observed data points are fitted with a cosine curve of the 4ϕ phase (dashed line), which ensures the correct MLD observation.

5.4. *Application to UV MCD PEEM*

Imaging photoelectrons provides detailed information of magnetic domain structures [39–44,64]. Magnetic domain images on Fe films [6] and NiO(001) crystals [65] have been reported previously using magnetic linear dichroism with a Hg lamp. On the contrary, MCD domain imaging using lasers has not been published. Figure 17 shows magnetic domains of Cs/Ni(10 ML)/Cu(001) observed by the MCD PEEM with second-order harmonics from a mode-locked Ti : sapphire laser excitation (800 nm). The magnetic image is obtained from the subtraction between the two images taken with positive and negative helicity light. The image clearly shows the MCD asymmetry and the average

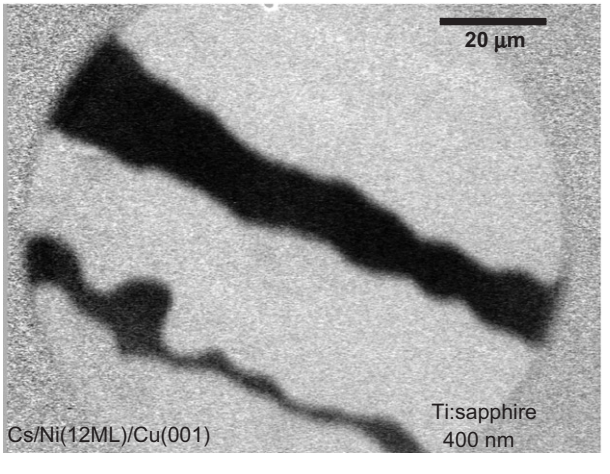

Figure 17. UV MCD PEEM image of Cs/Ni(12 ML)/Cu(001) taken by using a second harmonics of a Ti : sapphire laser (400 nm). Two images for positive and negative helicity light were recorded with the acquisition period of 2 s and were subtracted to yield the MCD image. From [5].

asymmetry is ~3%. The present MCD PEEM resolution is still a few hundred nm, which comes from inaccurate PEEM adjustment. However, the MCD PEEM combined with the present threshold photoemission technique may allow us to improve the spatial resolution [5], since the energy distribution of the photoelectrons is essentially narrower than that of the XMCD PEEM using synchrotron radiation soft X-rays.

6. Adsorbate induced spin reorientation transitions (SRT) in magnetic thin films

One of the most interesting issues in surface magnetism is the effect of the adsorbate for the magnetism. Especially, adsorbate-induced spin reorientation transitions (SRT) are striking since a small perturbation at the surface leads to a drastic change of the magnetization for whole metal films. In this section, several kinds of SRT induced by atomic and/or molecular adsorption will be surveyed after a brief description of magnetic anisotropy.

In order to determine quantitatively the magnetic anisotropy constants, the ferromagnetic resonance (FMR) technique is one of the most suitable methods since the resonance frequency is directly related to the magnetic energy as given in Equation (37) below. Readers are strongly recommended to refer to recent reviews on FMR, for instance, by Farle [66]. Moreover, recent theoretical development has enabled us to evaluate the magnetic anisotropy of ultrathin films including the absorbate effect, in spite of the fact that the magnetic anisotropy constants are usually much less than 1 meV. Readers can refer to a recent first principles calculation based on the full potential linearized augmented plane wave method [67]. Excellent agreement with the experimental magnetic anisotropy constants of oxygen-adsorbed Ni/Cu(001) has allowed us to discuss the adsorbate effect at the electronic structure level.

6.1. *Phenomenological origins of magnetic anisotropy*

Although phenomenological magnetic anisotropy has already been discussed partly in Section 3.3, we will here consider in a little more detail the SRT induced by adsorbates. For simplicity, let us assume infinite width of the metal thin film whose lateral (azimuthal) anisotropy can be neglected. The magnetic anisotropy energy $E_a(\theta_M)$, where θ_M is the polar angle of the magnetization, is phenomenologically described within the second-order approximation as

$$E_a(\theta_M) = \left(-\frac{N}{2\mu_0} M_S^2 + K_{2V} + \frac{K_{2S} + K_{2I}}{d}\right) \cos^2 \theta_M - \mathbf{H} \cdot \mathbf{M}_S, \tag{37}$$

where M_S the saturated magnetization, d the thickness of the film, and $\mathbf{H}$ the magnetic field. This formula is essentially the same as Equation (28), though the second-order anisotropy constant K_2 is separated into three parts K_{2V}, K_{2S} and K_{2I}, which denote the volume, surface and interface anisotropies, respectively. The first term in parentheses, $-NM_s^2/(2\mu_0)$, is the demagnetization energy due to the magnetic dipole–dipole interaction, where N is the demagnetization coefficient and is unity in the infinite width film. This term always stabilizes the in-plane magnetization and is called shape anisotropy. If the system favours perpendicular magnetic anisotropy (PMA), namely, if E_a is minimized at $\theta_M = 0$ when $\mathbf{H} = 0$, the quantity in parentheses should be positive. In the following subsections,

we will discuss the magnetic anisotropies of Ni/Cu(001), Co/Pd(111) and Fe/Ag(001), in which the positive magnetic anisotropy constants are known to be K_{2V}, K_{2I} and K_{2S}, respectively, thus leading to stabilization of the PMA at some thickness.

6.2. *Hydrogen adsorption on Ni/Cu(001)*

Ni/Cu(001) shows the SRT with a critical thickness d_C of ~10.5 ML. Below 10 ML, the film exhibits in-plane magnetization, while it shows PMA above 10 ML up to ~50 ML. Since PMA is usually observed when the films are thinner than a certain critical thickness, the present system is peculiar and thus interesting. This is caused by the positive volume magneto-elastic anisotropy ($K_{2V} > 0$) in Equation (37) [57,68]. The positive K_{2V} is derived from a tetragonal distortion of the Ni film that grows pseudomorphically on Cu(001) whose interatomic distance is slightly larger than the Ni one. Vollmer *et al.* [7] and van Dijken *et al.* [68] have investigated the SRT of ultrathin Ni films induced by adsorption of hydrogen, CO and Cu. Figure 18(a) exhibits polar MOKE asymmetry images of the same section of a Ni wedge on Cu(001) for five H_2 exposures at 143 K. The Ni thickness increases from the bottom to the top of the image as indicated by the scale on the left hand side. The bright area indicates the PMA region, while the dark area shows in-plane magnetization. The critical thickness is clearly found to be reduced upon H_2 adsorption down to ~6.8 ML at saturation adsorption. The stabilization of PMA is ascribed to a significant reduction of the magnetocrystalline anisotropy constant K_{2S}, which is −153 and −70 μeV/atom for the clean and H-adsorbed surfaces, respectively.

Sander *et al.* [69] further demonstrated reversible switching of the easy axis by changing the partial pressure of hydrogen. Figure 18(b) shows the switching behaviour of an 8 ML thick Ni film on Cu(001). When the hydrogen pressure $P(H_2)$ is too low, the Ni film has an in-plane easy axis of magnetization. By increasing $P(H_2)$ from 9.3×10^{-10} to 2.7×10^{-8} mbar, a remanent polar MOKE signal is detected, indicative of PMA. As indicated by the vanishing polar MOKE signal, subsequent reduction of $P(H_2)$ reverts the magnetization back to in-plane. This switching of the magnetization orientation is fully reversible as is apparent from the succession of polar MOKE signals in Figure 18(b), and it has to be correlated with the hydrogen pressure and coverage profiles in Figures 18(c) and (d). A quantitative LEED study of the diffracted intensity versus electron energy shows that the hydrogen induced SRT is accompanied by changes of the tetragonal distortion of the topmost Ni layer upon hydrogen adsorption. Surprisingly, the orientation switch to perpendicular to the surface comes with a relaxation: namely, reduction of the tetragonal distortion rather than its amplification.

Van Dijken *et al.* [68] also investigated Cu-capped Ni/Cu(001). Figure 18(e) shows the critical thickness d_C as a function of sample temperature for the clean (squares) and the Cu covered (circles and triangles) Ni/Cu(001) film. Growth of Cu on a Ni wedge also shifts the border of the SRT to smaller film thickness. At a Cu coverage of one monolayer the critical thickness is reduced by 3 ML with respect to the clean Ni surface. Further growth of Cu does not change the SRT any further. The shift of the data points towards higher values at about 350 K and above in Figure 18(e) is not due to the increase of the thickness at which the magnetization switches from in-plane to perpendicular magnetization but is attributed to the transition from the ferromagnetic to the paramagnetic phase. The displayed data points above 350 K, therefore, do not indicate the film thickness

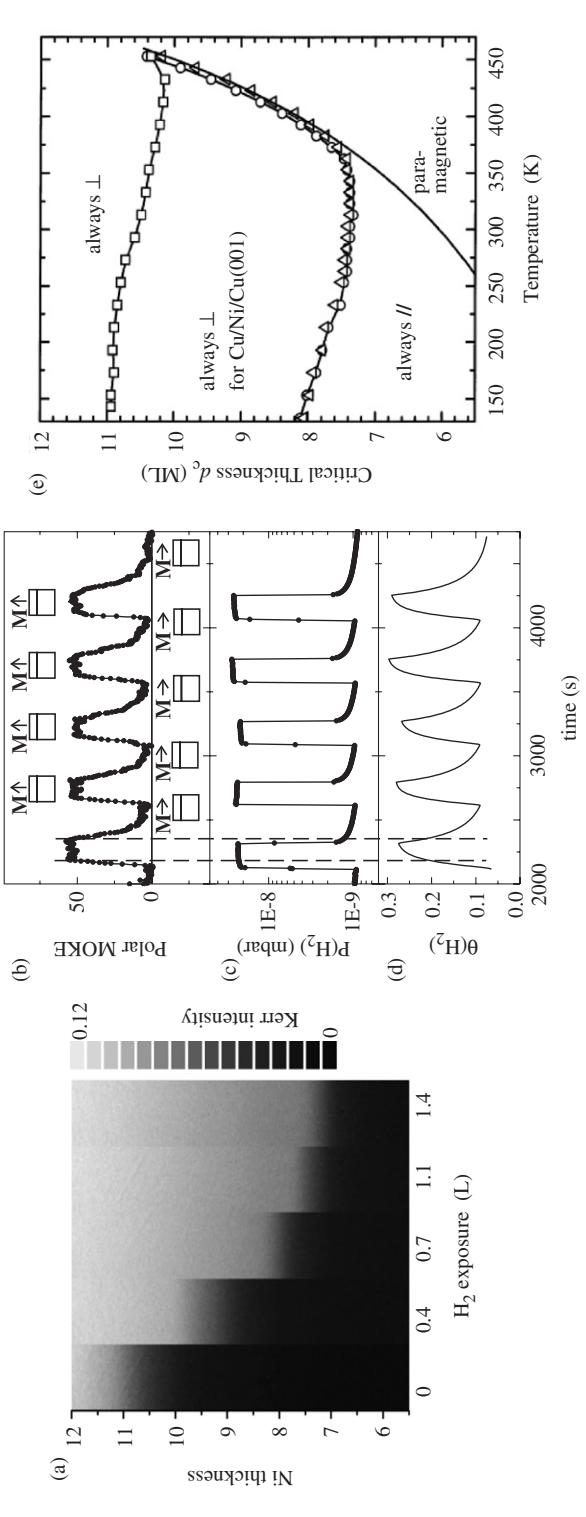

Figure 18. (a) Polar MOKE asymmetry images of the same section of a Ni wedge on Cu(001) for five H_2 exposures at a temperature of 143 K. The Ni thickness increases from the bottom to the top of the image as indicated by the scale on the left hand side. The bright area indicates the presence of perpendicular magnetization, the dark area in-plane magnetization. From [7]. (b) H-induced variation of the polar MOKE signal of Ni(8 ML)/Cu(001) at 322 K. The switching of the easy axis of magnetization from in plane, $M^{//}$, to perpendicular to the Ni film, $M^{\perp}$, due to a $P(H_2)$ variation, as displayed in panel (c), is apparent. The time delay between the signals is caused by the dynamics of the H-adsorption process. (d) Calculated coverage of hydrogen $\theta(H_2)$ for the pressure variation of (c). The broken lines indicate that at $\theta(H_2) = 0.23$ the magnetization direction switches from in plane to out of plane and back. From [69] for (b)–(d). (e) Critical thickness of the spin reorientation transition of the clean Ni surface (squares) and the Ni surface capped with 2 ML Cu (triangles) and 5 ML Cu (circles). The solid line is a power law $T_C(d)/T_C(\infty) = 1 - (d/d_0)^{-\lambda}$ with $T_C(\infty)$ the bulk Curie temperature, $d_0 = 3.6$ ML and $\lambda = 1.2$. From [68].

at which the reorientation from perpendicular magnetization to in-plane magnetization occurs. They mark the boundary where the out-of-plane remanent magnetization disappears instead. The solid line in Figure 18(e) is a power law $T_C(d)/T_C(\infty) = 1-(d/d_0)^{-\lambda}$ with $T_C(\infty)$ the bulk Curie temperature, $d_0 = 3.6$ ML and $\lambda = 1.2$. The surface magnetocrystalline anisotropy constant is consequently obtained as $K_{2S} = -83$ μeV with $d_C = 7.4$ ML. The effect of adsorbate is a little smaller than the hydrogen case and similar to the CO adsorption case of $d_C = 7.3$ ML and $K_{2S} = -81$ μeV.

6.3. *CO adsorption on Co/Pd(111)*

6.3.1. *Co L-edge XMCD*

The Co/Pd(111) film shows PMA when the film thickness is thinner than $d_C \sim 3.5$ ML [70,71], the situation being different from that of Ni/Cu(001). The origin of PMA is ascribed to positive interface magnetic anisotropy ($K_{2I} > 0$). Matsumura *et al.* [72] investigated the SRT of Co/Pd(111) upon CO adsorption. Figure 19(a) shows the Co $L_{III,II}$-edge XMCD spectra of clean and CO-adsorbed 4.5 ML Co films grown on Pd(111) taken at 200 K. As indicated in the clean one, the easy axis of the films lies parallel to the surface and no XMCD signal is observed at $\theta_{in} = 0°$ (normal X-ray incidence). By dosing the Co film with saturated amounts of CO at 200 K, the spectra have changed drastically.

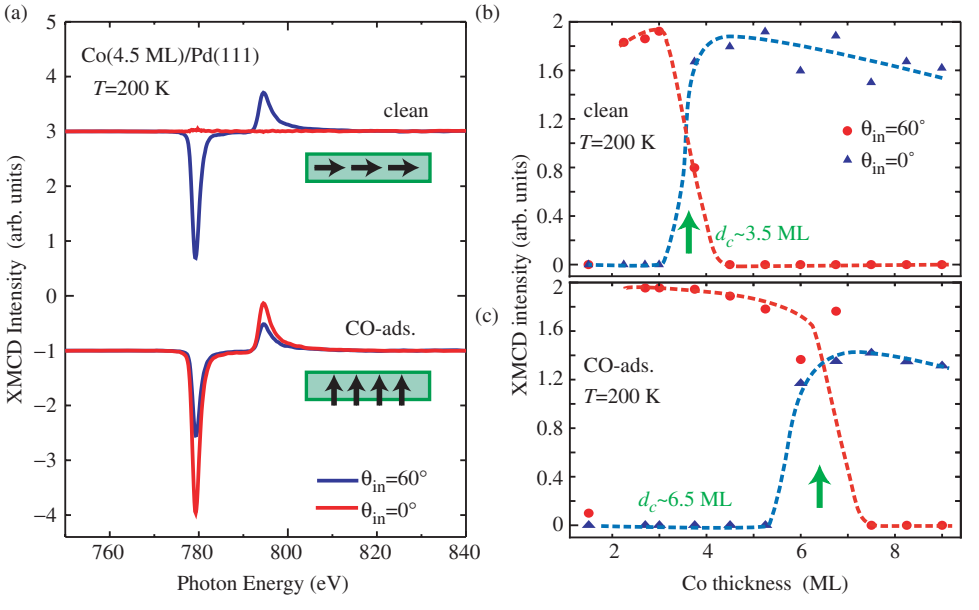

Figure 19. [Colour online] (a) Co $L_{III,II}$-edge circularly polarized and XMCD spectra of a clean and CO-adsorbed 4.5 ML Co film on Pd(111) taken at 200 K and X-ray incident angles of $\theta_{in} = 60°$ (grazing) and $\theta_{in} = 0°$ (normal). (b) XMCD intensity (scaled as effective spin magnetic moments) of clean and CO-covered Co films on Pd(111) at 200 K as a function of Co thickness. Circles and solid lines correspond to the surface normal direction, while triangles and dashed lines correspond to the surface parallel one. Hatched areas indicate the PMA region. From [72].

The XMCD signal appears at $\theta_{in} = 0°$, implying the occurrence of SRT by CO adsorption. Figure 19(b) shows the XMCD intensity (corresponding to the effective spin magnetic moments) at 200 K with various Co thicknesses for the surface normal and parallel directions. Below ~3 ML, the film shows PMA, while above ~4 ML the film exhibits in-plane magnetization. Thus, the critical thickness is ~3.5 ML, the same as it was for 300 K in the previous literature [70]. The 1.5 ML Co film shows no magnetization in either direction, implying the Curie temperature below 200 K. On the other hand, the CO-adsorbed films thinner than ~6.5 ML exhibit PMA. The critical thickness increases by ~3 ML compared to that of clean surface films ~3.5 ML. It should be noted that no shift in the critical thickness was observed for CO adsorption at 300 K, this being discussed later. A similar SRT was reported in CO adsorption on Co/Pt(111) at low temperature [73].

To provide a more detailed understanding of the SRT, Figure 20(a) shows changes in the orbital magnetic moments in Co/Pd(111) induced by CO exposure at 200 K. From the viewpoint of the magnetic easy axis, we can classify Co thickness into three regions. Below 3 ML, Co films always show PMA even before CO adsorption (region I). Above 7 ML, on the other hand, Co films show in-plane magnetization even after CO adsorption (region III). In the thickness range between 3 and 7 ML, Co films exhibit the SRT (region II).

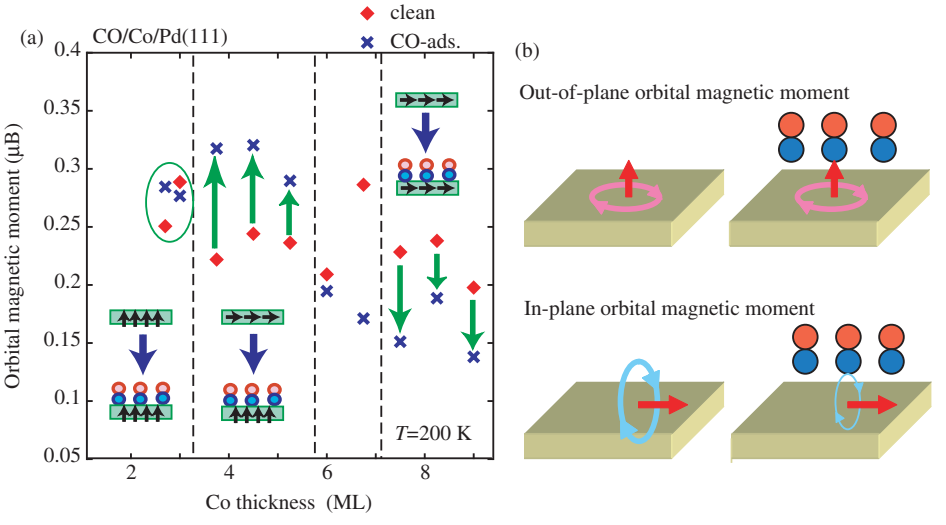

Figure 20. [Colour online] (a) Orbital magnetic moments of the Co films on Pd(111) at 200 K as a function of Co thickness. Diamonds and crosses denote clean and CO-adsorbed Co, respectively. Note that there exists a mixture phase between regions II and III, where the perpendicular or parallel orbital moment is poorly defined. (b) Schematic pictures of the orbital moments of surface atoms. Rotating arrows indicate the rotation of the 3*d* electrons, and straight arrows indicate corresponding orbital angular momenta. A parallel orbital moment is always favoured over a perpendicular one for the atoms in the topmost layer of the clean surface. Upon CO adsorption, the perpendicular orbital moment, which originates from the electron rotation in the surface plane, is almost unchanged, because the CO molecules are standing up at the atop site, while the parallel orbital moment due to the out-of-plane rotation of the electrons is significantly quenched because of the hindrance of CO at the surface. From [72].

As seen in region I, the perpendicular orbital magnetic moments are left unchanged upon CO adsorption. In region II, the orbital magnetic moment after CO adsorption (PMA) is greater than that before CO adsorption (parallel). In region III, adsorption of CO causes significant reduction of the in-plane orbital magnetic moments. Shape anisotropy, $-M_s^2/2\mu_0$ in Equation (37), always favours in-plane magnetization because of the classical magnetic dipole–dipole interaction. Let us discuss the quenching mechanism of the orbital magnetic moments in the in-plane direction upon adsorption. When the in-plane orbital moment of the surface atoms is reduced, surface magnetocrystalline anisotropy is suppressed, leading to the stabilization of PMA, as in the above Ni/Cu(001) case. Schematic pictures of the orbital moments of the surface atoms are depicted in Figure 20(b). The perpendicular orbital moment, which is derived from in-plane orbitals, is barely quenched. On the other hand, out-of-plane electron orbitals, which induce the in-plane orbital moment, interact with CO strongly, leading to significant quenching of the in-plane orbital moment. This picture can be applied to both the CO-adsorbed Co/Pd(111) and Ni/Cu(001) films. In CO/Co/Pd(111), this effect causes almost no change in the perpendicular orbital moment in region I, but significant suppression of the in-plane orbital moment by CO reduces the absolute value of surface magneto-crystalline anisotropy K_{2S}, leading to the stabilization of PMA.

6.3.2. *C 1s X-ray photoelectron spectra (XPS) and photoelectron diffraction*

Matsumura *et al.* [74] further studied the relation between the drastic magnetization switching and the adsorbate structure. In Figure 21(a), C 1*s* X-ray photoelectron spectra (XPS) of CO adsorbed on Co/Pd(111) taken at 300 and 200 K are shown. Note that CO adsorption induces SRT at 200 K, while does not at 300 K. The spectrum at 300 K is well reproduced by a single Voigt function, suggesting a single site adsorption of CO. On the other hand, the spectrum taken at 200 K has an additional shoulder at 285.3 eV. This implies that there are two or more kinds of adsorption sites at 200 K. Figure 21(b) shows the photoelectron diffraction images for CO adsorbed on Co/Pd(111) at 300 K. The mapping corresponds to the probability density of the nearest neighbour substrate Co atoms. These results clearly indicate that CO is adsorbed on atop site of the Co thin film. The quantitative analysis of the scanned-energy photoelectron diffraction modulation functions taken at five different emission directions yields the C–Co interatomic distance of 1.78 Å. For CO adsorption at 200 K, Figure 21(c) shows similar images. The image of the YZ section at $X = 0.0$ Å [left panel in Figure 21(c)] clearly indicates several adsorption sites. The image of the XY plane at $Z = -1.85$ Å is ascribed to the atop adsorption, while that at $Z = -1.70$ Å uniquely to the bridge site adsorption. Note that if CO were adsorbed in the hollow site, six spots should appear at the positions rotated by 30° from the observed ones.

6.3.3. *Correlation between Co L-edge XMCD and C 1s XPS*

Figures 22(a) and (b) shows C 1*s* photoelectron and Co XMCD spectra from the 4.5 ML Co thin film on Pd(111) measured alternatively after each step of CO exposure at 200 K [74]. Note that in Figure 22(b), the X-ray incident angle for the XMCD measurements was set to normal ($\theta_{in} = 0°$) so as to detect the perpendicular component of the magnetization. Before CO dosage, we confirmed that the Co thin film was fully magnetized in the surface

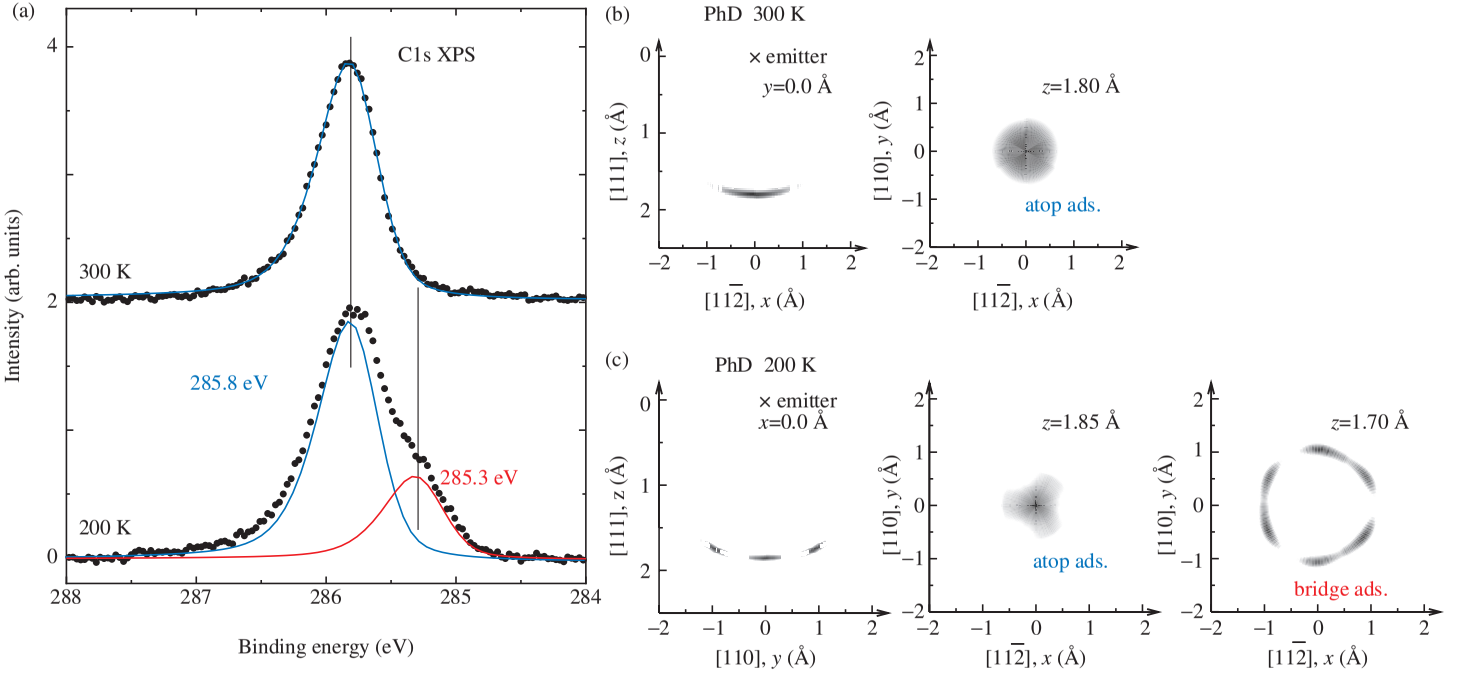

Figure 21. [Colour online] (a) C 1*s* X-ray photoelectron spectra of CO/Co(4.5 ML)/Pd(111), taken at 200 and 300 K. Peak positions are marked by vertical lines. The shoulder at 285.3 eV is only observed in the spectrum at 200 K. (b) Images of the nearest-neighbour Co atoms from the C emitter for CO/Co(5 ML)/Pd(111) at 300 K, obtained by the projection method. Top figure is in a section through the surface and bottom figure is in a plane parallel to the surface 1.80 Å below the C emitter. (c) Similar images for 200 K. Left figure is in a section through the surface. Middle and right panels are in planes parallel to the surface 1.85 and 1.70 Å below the C emitter, respectively. From [74].

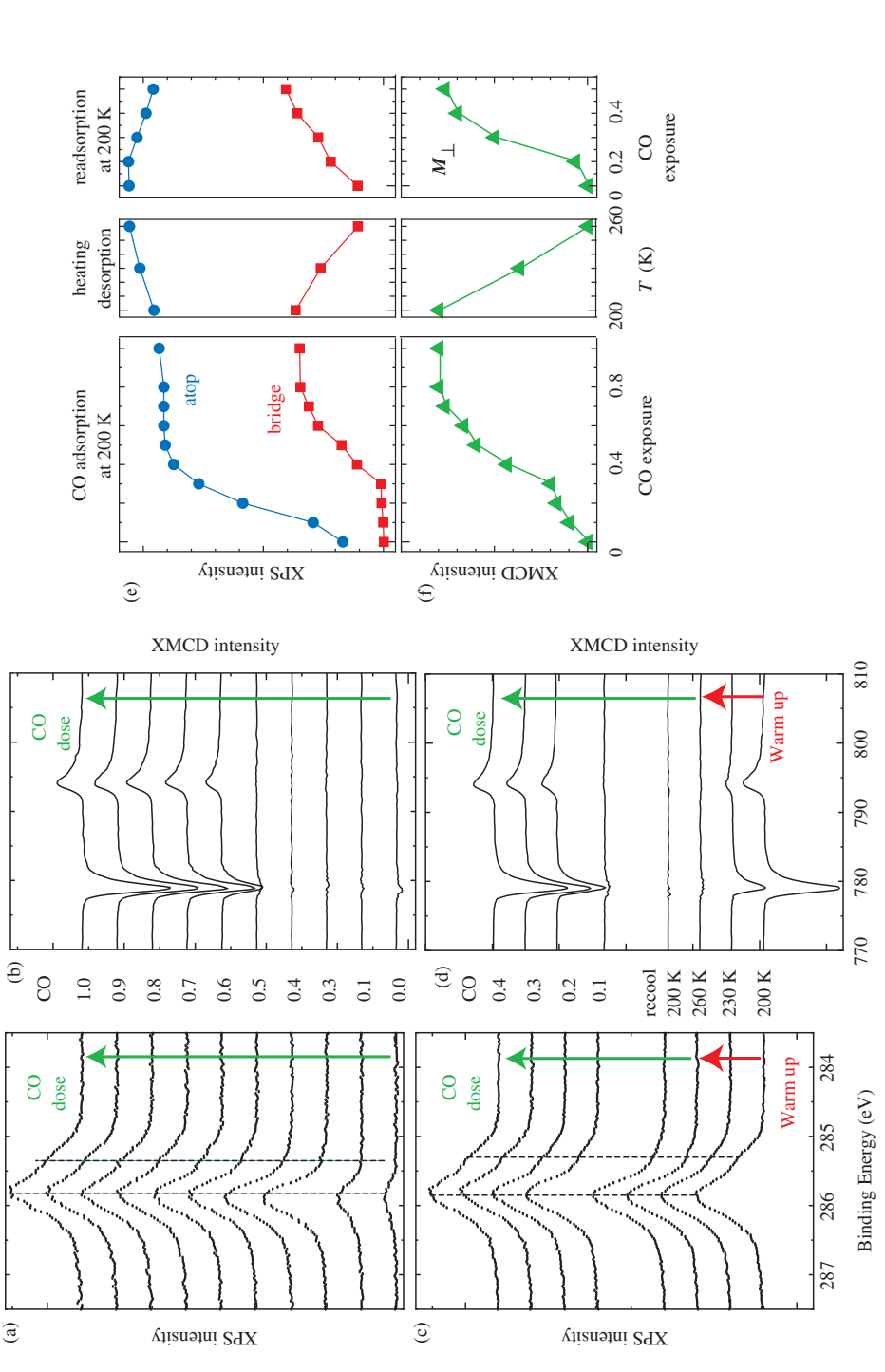

Figure 22. [Colour online] (a), (b) C 1*s* photoelectron (a) and normal incidence Co *L*-edge XMCD (b) spectra from 4.5 ML Co film on Pd(111) as a function of the CO effective exposure at 200 K. (c), (d) C 1*s* photoelectron (c) and normal incidence Co *L*-edge XMCD (d) spectra from 4.5 ML Co film on Pd(111) during heating desorption from 200 K and readsorption at 200 K. (e) C 1*s* XPS peak intensities assigned to the atop (blue circle) and bridge (red square) sites, together with the Co L_{III} XMCD peak intensity (green triangle) for the 4.5 ML Co film on Pd(111) during step by step CO adsorption at 200 K (left), desorption by annealing (middle) and readsorption at 200 K (right). From [74].

parallel direction by the XMCD observation at grazing incidence. Thus, the nearly zero XMCD signal at low CO coverages means that the Co thin film is fully magnetized in the in-plane direction. The Co film undergoes a SRT from surface parallel to perpendicular magnetization after CO saturated adsorption. In the CO adsorption process, we define an effective exposure of 1.0 at the saturation exposure. At the early stage of CO exposure, as long as CO occupies only atop site, Co is in-plane magnetized. At around 0.5 exposure, the shoulder at 285.3 eV starts to grow in XPS. Simultaneously, the XMCD signal gradually appears. This means that the magnetization axis begins to change from the surface parallel to perpendicular direction. At ~1.0 exposure, the intensities of both C 1*s* and Co XMCD spectra are saturated, indicating that the SRT was completed in the entire film with saturated CO adsorption. No further change was found in either XPS or XMCD above 1.0 exposure.

Next, we will look at the CO desorption process of the same film. As shown in Figures 22(c) and (d), the shoulder at 285.3 eV of the C 1*s* spectrum gradually decreases by annealing, accompanied with the disappearance of the Co XMCD, while the C 1*s* main peak intensity remains almost constant. The SRT from the surface perpendicular to parallel magnetization is completed at 260 K, where the shoulder has disappeared in the XPS. When cooling back to 200 K, the Co XMCD does not recover its intensity and the Co thin film keeps its in-plane magnetization. This experiment clearly shows that the SRT caused by the annealing is ascribed not to a temperature effect but to a pure desorption effect of CO adsorbed on the bridge site. Although the change of the Curie temperature induced by the desorption can influence the thermodynamic parameters of the magnetic anisotropy, this effect can be neglected because the Co thin film shows nearly saturated magnetization at room temperature even at a thickness of 2 ML. Adsorption of CO again at 200 K after annealing and cooling recovers the shoulder at 285.3 eV in XPS and a certain signal of XMCD. CO was adsorbed on the bridge site in this case. This behaviour was found to be reproducible at least for several time repetitions.

For a clearer view, the two contributions in the C 1*s* spectra are resolved by a curve fitting procedure. Figures 22(e) and (f) show the intensities of the XPS peaks corresponding to both atop and bridge sites with the Co L_{III} XMCD peak intensity as functions of CO dosage and annealing temperature. It is recognized that the SRT is induced only by CO adsorbed on the bridge site. Now, we understand why the previous experiments of CO adsorption at 300 K did not detect the shift of the critical thickness of Co/Pd(111). The substrate temperature was too high to adsorb CO on the energetically unfavoured bridge sites. If the substrate temperature is low enough to adsorb CO on the bridge site, the surface magnetic anisotropy is drastically changed and the critical thickness shifts. It is amazing that, although the quantity of CO adsorbed on the atop site is three times as large as that on the bridge site at 200 K and the bonding between CO and Co is weaker at 200 K than at 300 K, the atop site occupation does not alter the critical thickness and the bridge site occupation shifts the critical thickness by ~3 ML.

6.3.4. *Discussion on magnetic anisotropy*

In contrast to Ni/Cu(001), Co layers on Pd(111) retains bulk lattice spacing that is essentially different from the Pd substrate. Although the strong interface magnetocrystalline anisotropy favours the out-of-plane magnetization [71], the bare Co/Pd(111) exhibits

the in-plane magnetization above 3.5 ML thickness of Co. For the multilayer Co/Pd(111) systems, the critical thickness has been reported to be about 9 ML [75]. If the magnetic anisotropy of the Co film mainly originates at the surface or interface, one can estimate the surface magnetocrystalline anisotropy K_{2S} from the critical thickness of the bare Co/Pd(111) and the multilayer system. By using the reported interface magnetocrystalline anisotropy, $K_{2I} = 300$ μeV/atom [75], K_{2S} is estimated to be -67 μeV/atom. On the other hand, since the critical thickness of CO/Co/Pd(111) is 6.5 ML at low temperature, K_{2S} for the CO adsorbed Co film is similarly estimated to be 133 μeV/atom. Thus, the bridge site CO adsorption changes K_{2S} by $+200$ μeV/atom. It is intriguing to consider why the simple atop adsorption does not, while atop and bridge sites adsorption induces the SRT. One possible explanation is as follows. CO adsorption on the atop site gives little effect on the Co surface geometry, while it is likely that CO adsorbed in the bridge site pushes the bonding Co atoms away and elongates the in-plane interatomic Co distance, which in turn compresses the neighbouring Co–Co atomic distances. Such structural change might enhance the out-of-plane anisotropy of the top layer. Other possibilities such that CO saturated adsorption plays a key role for the structural change cannot be excluded, which favours PMA.

6.4. *Oxygen and NO adsorption on Fe/Ag(001)*

The third example is the Fe/Ag(001) system, which shows PMA below ~3 ML. Chen *et al.* [76] found that oxygen adsorption on Fe/Ag(001) induces the *destabilization* of PMA, the behaviour of which differs from the previous two examples of Ni/Cu(001) and Co/Pd(111). They concluded that the thin film anisotropy of Fe/Ag(001) is dominated by spin–orbit contributions that govern the surface anisotropy parameter, while the structure flattening reconstruction effect due to oxygen adsorption is not a driving force for the change of magnetization direction. Recently, Ma *et al.* [77] studied oxygen and NO adsorption on Fe/Ag(001) including the XMCD measurements.

6.4.1. *MOKE and Fe L-edge XMCD*

Figure 23(a) shows the magnetic hysteresis curves taken by the polar and longitudinal MOKE measurements of the 2.2 ML Fe film on Ag(001) with O_2 adsorption at 100 K. Oxygen is dissociated to atomic oxygen on Fe/Ag(001). The clean Fe film exhibits hysteresis only in the polar MOKE with the coercive field H_C of ~100 Oe. The hysteresis looks almost rectangular, and the magnetic easy axis is the surface normal. Upon 0.12 L O_2 exposure, the polar MOKE turns to a smoother curve with $H_C \sim 40$ Oe, and the longitudinal MOKE appears with an almost rectangular shape ($H_C \sim 50$ Oe). Upon 0.4 L O_2 exposure, no polar MOKE signal was detected and the longitudinal MOKE gives an almost rectangular hysteresis loop with $H_C \sim 30$ Oe. The magnetic easy axis is in the surface plane, and the SRT was actually reproduced as in the previous work by Chen *et al.* [76]. Oxygen adsorption is confirmed to destabilize the PMA, the consequence being different from those of H/Ni/Cu(001) and CO/Co/Pd(111). It is also noted that the coercive fields in both the perpendicular and in-plane magnetization processes are noticeably larger in the mixed region of 0.12 L O_2 exposure than in the perfectly perpendicular or in-plane magnetized films with the same thickness.

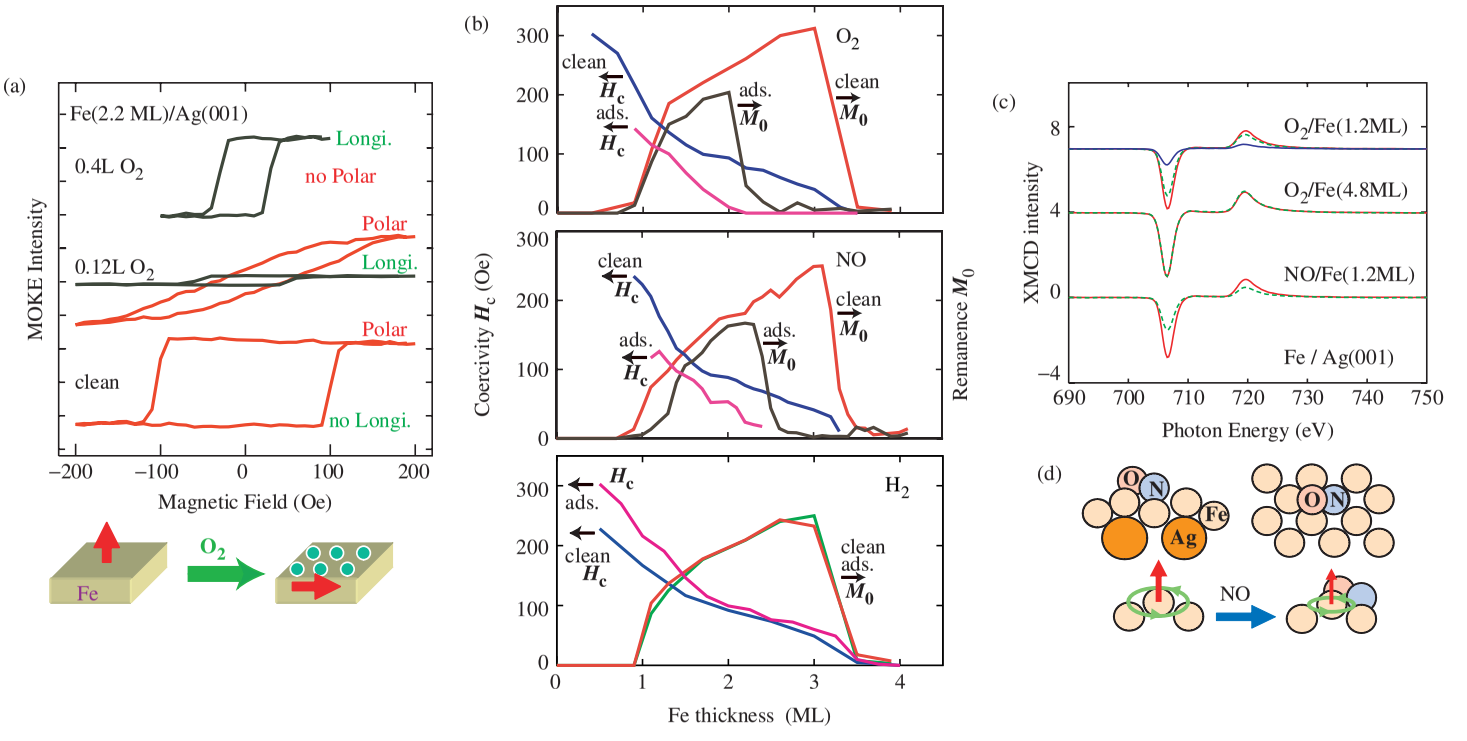

Figure 23. [Colour online] (a) Magnetization curves taken at 100 K by the polar and longitudinal MOKE measurements for clean and O-adsorbed Fe (2.2 ML) films on Ag(001). The flat Fe film was used. (b) Remanent magnetization and the coercive field of the Fe films on Ag(001) before and after gas (O_2, NO and H_2) adsorption recorded at 100 K by the polar MOKE measurements. The wedge-shaped Fe film was used. (c) Fe $L_{III,II}$-edge XMCD of clean (red solid lines) and adsorbed (green dashed and blue solid lines) Fe films on Ag(001), taken at normal X-ray incidence (1.2 ML) and grazing X-ray incidence (4.8 ML) at 100 K. The amounts of gas dosage are as follows: for O_2/Fe(1.2 ML)/Cu(001), green dashed: 0.05 L and blue solid: 0.15 L, for O_2/Fe(4.8 ML)/Cu(001): 0.15 L O_2, and for NO/Fe(1.2 ML)/Cu(001) green dashed: 0.1 L NO. (d) Quenching mechanism of the orbital magnetic moment by NO adsorption on Fe/Ag(001). Rounded green arrows represent the rotational motions of 3*d* electrons, while thick straight red arrows the orbital magnetic moments. Because of the flat lying NO adsorption, the out-of-plane orbital angular momentum caused by the in-plane electron rotation is more effectively quenched. From [77].

Figure 23(b) shows the Fe thickness dependence of the remanent magnetization and the coercive field before and after gas adsorption obtained by the polar MOKE measurements of the wedge-shaped Fe films at 100 K. In the cases of O_2 and NO adsorption, the critical thickness d_C for the spin reorientation transition is found to shift to a thinner side: the critical thicknesses of ~3.4, ~2.3 and ~2.5 ML for clean, O- and NO-adsorbed films, respectively. The finding for O_2 adsorption is consistent with the previous work [76]. For these two gases, the coercive fields are suppressed after adsorption. In contrast, H_2 adsorption shows a different effect on magnetic anisotropy. No critical thickness shift is detected even after 5 L dosage of H_2. The remanent magnetization is not suppressed, while the coercive field is enhanced. These findings are essentially dissimilar to the O_2 and NO adsorption cases.

Figure 23(c) shows the Fe $L_{III,II}$-edge XMCD. The XMCD intensity noticeably decreases with the oxygen dosage in the 1.2 ML Fe film. NO adsorption on 1.2 ML Fe shows a similar behaviour. Note that only the effective spin magnetic moments $m_{spin}^{eff} = m_{spin}^{eff} + 7m_T$ are obtained in this experiment. Ohresser *et al.* [78] investigated the contribution of the magnetic dipole term m_T compared to the spin magnetic moment in the Fe nanoclusters and ultrathin films on Au(111) by using a 7 T superconducting magnet. They concluded that in the Fe film thicker than 2 ML the magnetic dipole term is not negligible. In the 1.2 ML Fe films, the ratio of $7m_T/m_{spin}^{eff}$ is estimated as ~0.1. We should note that the effective spin magnetic moments for the 1.2 ML films investigated here are roughly by 10% overestimated. The *d* hole number of the clean 1.2 ML Fe film is 3.73 ± 0.10, which is noticeably larger than the one of the clean 4.8 ML Fe film ($d_{hole} = 3.40$). Moreover, the ratio of the orbital/spin magnetic moments, m_{orb}/m_{spin}^{eff}, is enhanced in a thinner film: $m_{orb}/m_{spin}^{eff} = 0.075 \pm 0.010$ for the 1.2 ML Fe and $m_{orb}/m_{spin}^{eff} = 0.036 \pm 0.004$ for the 4.8 ML Fe. The effective spin magnetic moment of the clean 1.2 ML Fe film is, on the contrary, $2.35 \pm 0.15\,\mu_B$, which is smaller than that of the clean 4.8 ML Fe film $2.65 \pm 0.10\,\mu_B$. The effects of O_2 and NO adsorption are quite similar to each other. The spin magnetic moments are reduced, while the *d* hole number increases. More interestingly, the ratios of the orbital/spin magnetic moments, m_{orb}/m_{spin}^{eff}, are also suppressed. This implies that the orbital magnetic moment is quenched more rapidly than the spin magnetic moment. On the other hand, the effect of H_2 adsorption is again found to be quite small when one compares the spin magnetic moment and the ratio of the orbital/spin magnetic moments.

6.4.2. *Discussion on magnetic anisotropy*

Chen *et al.* [76] clarified that adsorption of O_2 on the Fe film on Ag(001) destabilizes the PMA. This may be a unique example since all the other films lead to the *stabilization of PMA* on adsorption: H_2 and CO on Ni/Cu(001), CO on Co/Pd(111), Cu on Ni/Cu(001) and so forth. This is because all the latter systems give negative surface magnetocrystalline anisotropy that favour the in-plane magnetization and are weakened on adsorption on the surface. On the other hand, the present Fe/Ag(001) system has a positive surface anisotropy constant ($K_{2S} > 0$) [72], which is similarly suppressed on gas adsorption. In the cases of O_2 and NO adsorption on Fe/Ag(001), the surface anisotropy is reduced, leading to the destabilization of PMA, while in the case of H_2 the interaction is too weak to shift the critical thickness. Chen *et al.* [76] discussed the microscopic origin for the destabilization of PMA in O_2 adsorption. They observed the sharpening of the LEED

spot after O_2 adsorption and speculated that the surface roughness of the Fe film is noticeably reduced by O_2 adsorption. Although the flattening of the film may induce the destabilization of the PMA, they supposed that the destabilization of PMA originates from the changes of the spin–orbit interaction, but they gave no information on the orbital magnetic moment. This is partly the reason why the effect of O_2 adsorption is reinvestigated by means of the XMCD, which yields the orbital magnetic moment directly. Actually, it is found that the perpendicular orbital magnetic moment is quenched more significantly than the perpendicular spin magnetic moment upon O_2 and NO adsorption. It is concluded that the quenching of the perpendicular orbital magnetic moment plays a key role for the destabilization of PMA.

An illustration regarding the variation of the orbital moments with different adsorption geometries is given here for better understanding. In the case of CO adsorption on Co/Pd(111) and Ni/Cu(001), as shown in Figure 23(d), it was found that the perpendicular orbital magnetic moments do not change so much upon gas adsorption. This is in clear contrast to the present system and is the reason for the different behaviours of the stabilization or destabilization of PMA. This should be ascribed to a different geometric configuration during gas adsorption. In the previous systems, CO adsorbs with the molecular axis perpendicular to the surface. This geometry interrupts the in-plane orbital magnetic moment more efficiently than the perpendicular moment since the perpendicular orbital magnetic moment originates from the electron rotation within the surface plane, which interacts with the adsorbate less strongly compared to the electron motion out of the surface plane. In the present case, however, the gas atom displays a geometric configuration that easily generates lateral interaction between adsorbents and Fe atoms. This lateral interaction tends to hamper the electron rotation within the surface that favours PMA.

A sketch of the adsorption model is given in Figure 23(d). The oxygen atom is usually located at the fourfold hollow site on the topmost Fe layer [76] but is noticeably embedded in the first Fe layer in the current case because *bcc* Fe(001) has a larger unit cell than *fcc* Co(111) or *fcc* Ni(001). The lateral interaction between the adsorbents and substrate thus becomes important and consequently the perpendicular orbital magnetic moment is efficiently quenched. In NO adsorption on Fe, Suzuki *et al.* [79] claimed that the NO molecular axis was highly tilted or even lying-down on the Fe surface. Another support for this structure model is the existence of a similar molecular axis tilting or lying-down observed in CO adsorption on Fe (001) surface [80,81]. This configuration of NO may induce strong lateral interaction and therefore suppress the in-plane electron motion that contributes to the perpendicular magnetic orbital moment. In contrast to O_2 and NO, H_2 shows almost no effect on the shift of critical thickness. This is due to a fact that the tiny hydrogen atom is always located on the top of the second Fe layer, which brings negligible lateral interaction with topmost Fe atoms.

6.5. *Cu, Ag and NO adsorption on Co on vicinal Cu(001)*

As a last example of SRT, Cu, Ag and NO adsorption on Co films on vicinal Cu(001) surfaces is discussed [52,82–86]. Step surfaces bring additional magnetic anisotropy within the surface plane since the directions parallel and perpendicular to the step edge are no longer equivalent. It is found that Co on stepped Cu(001) surfaces gives a magnetic easy

axis parallel to the step [82]. As shown below, a double hysteresis loop is observed along the direction perpendicular to the step, while a normal rectangular shaped hysteresis is detected along the easy axis. The double hysteresis loop is phenomelogically attributed to the magnetic anisotropy from atoms located at step sites [83]. From a microscopic point of view, Dhesi *et al.*[86] evaluated the spin–orbit coupling in Co on vicinal Cu(001) by means of the XMLD measurements. They showed that the spin–orbit coupling parallel to the step is larger than the one perpendicular to the step and gave a quantitative comparison between the anisotropic spin–orbit coupling and magnetocrystalline anisotropy.

6.5.1. *Cu adsorption on Co/Cu(1 1 41)*

Weber *et al.* [84,85] discovered adatom induced SRT on Co/Cu(1 1 41) from the parallel step to the perpendicular step direction. Figure 24(a) shows a spin-SEM (scanning electron microscopy) magnetic imaging of 12 ML Co partially covered with Cu (>1.2 ML). The entire image except one stripe appears dark. This is direct evidence that the magnetization

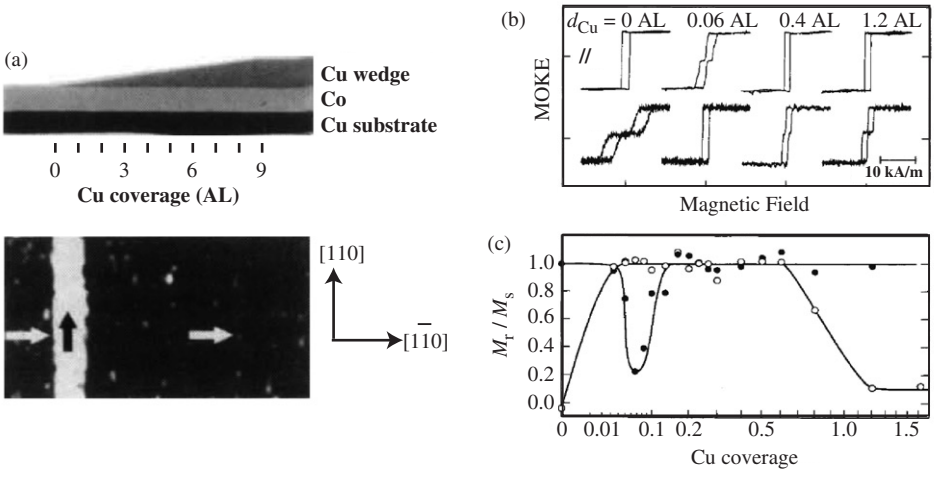

Figure 24. (a) (bottom) Spin-SEM image ($180 \times 60\,\mu m^2$) of a 12 ML Co film on a slightly miscut Cu(001) crystal with a Cu wedge (0–9 ML). (top) Cross-section through the sample. The arrows on the spin-SEM image indicate the magnetization direction of the Co film. The spin-SEM image shows a sharp transition of the magnetization direction, from parallel to the step to perpendicular to the step. (b) (top) Magnetization curves recorded by the longitudinal MOKE on a 12 ML Co film covered sequentially with Cu. Loops for the directions both parallel (∥) and perpendicular (⊥) to the steps of the miscut sample are shown at selected Cu thicknesses d_{Cu}. The rectangular loop is characteristic of the easy magnetization axis, whereas a more complicated loop composed of two smaller loops is observed in the other direction. (middle) The ratio of remanent magnetization MR to the saturated magnetization MS as a function of Cu coverage for both directions (∥solid circles; ⊥open circles; lines to guide the eye). The in-plane switching from parallel to perpendicular occurs at 0.03 ML, the switching back from perpendicular to parallel at 1.2 ML. The intermediate thickness range between 0.15 and 1.2 ML is a metastable state; the remanent magnetization stays in the direction in which the field was previously applied. As the wedge sample was measured as-grown in zero magnetic field, no switching of the magnetization direction at 0.15 ML was observed in the spin-SEM experiment in Figure 24(a). From [84].

of the Cu-uncovered as well as the Cu-covered (>1.2 ML) of the Co film points in the [1$\bar{1}$0] axis, which runs parallel to the steps induced by the miscut of the substrate. In contrast, at low Cu coverages the magnetization direction changes in-plane by 90° from [1$\bar{1}$0] to [110] (hereafter denoted parallel step and perpendicular step, respectively), as indicated by the light stripe. A line scan through the magnetic image reveals that this transition of the magnetization direction by 90° is discontinuous. This abruptness, and the fact that the original magnetization direction is resumed on further Cu coverage, signifies the elementary features of a magnetic switch: the magnetization switches discontinuously between two discrete states. Figure 24(b) exhibits the longitudinal MOKE on increasing the Cu coverage. Again the easy magnetization axis of the uncovered and the Cu-covered (>1.2 ML) Co films is directed to parallel step, and a more complicated one composed of two shifted loops for perpendicular step. Correspondingly, the ratio of the remanent magnetization M_R to the saturated magnetization M_S is $M_R/M_S = 1$ for the parallel step direction while $M_R/M_S = 0$ for the perpendicular step direction.

6.5.2. *Ag adsorption on Co/Cu(1 1 17)*

Nakagawa *et al*. [52] investigated MOKE, MSHG and XMCD of Ag adsorption on Co films on stepped Cu(001) surfaces. The results of MSHG were already described in Section 4.3. Figure 25(a) shows a model surface structure of Co/Cu(1 1 17). The terrace is 8.5 atom wide, and is separated by a monatomic step. The Co atoms are classified into four kinds: bulk, surface, step corner, and step edge atoms [83]. For the Co/Cu(1 1 17) film, the parallel step direction is known as a magnetic easy axis, the perpendicular step direction is a hard axis, and the direction perpendicular to the surface is the hardest axis. Figures 25(b) and (c) show the experimentally observed LEED patterns before and after Co deposition, respectively. The fundamental spots clearly split into two after Co deposition as well, confirming that the Co film grows in a layer-by-layer fashion and the step edge is maintained on the Co film surface.

Figure 25(d) show the MOKE magnetization curves on clean Co on Cu(1 1 17). The curve along the parallel step direction is a simple rectangular shape, while the perpendicular one shows zero remanence and a double hysteresis loop with the shift field of ~220 Oe. This is consistent with the above result by Weber *et al*. [84,85] and implies that the parallel step direction is an easy axis.

Figure 25(e) shows the Co *L*-edge XMCD spectra of 3 ML Co on Cu(1 1 17) with **M**//step and **M**⊥step. As seen in the L_{III} edge around 779 eV in Figure 25(b), the parallel step intensity is larger than the perpendicular step one, while the L_{II}-edge XMCD intensities are nearly the same. The larger L_{III} XMCD is ascribed to a larger orbital magnetic moment in the parallel step direction than that in the perpendicular step direction. A quantitative sum-rule analysis yields the orbital and effective spin magnetic moments, m_{orb} andm_{spin}^{eff}. The numerical results of the ratio m_{orb}/m_{spin}^{eff} are indicated in Figure 25(d). Although the difference of the ratio between the parallel step and perpendicular step directions is also not so significant, the parallel step direction shows larger orbital magnetic moments, as can be expected from the spectra. The present finding is consistent with the fact that the magnetic easy axis is parallel to the step edge.

Figure 25(f) show the magnetization curves recorded by the longitudinal MOKE of Ag(1 ML)-deposited 5 ML Co on Cu(1 1 17). In contrast to the results of the clean Co films, the perpendicular step magnetization curve shows a simple rectangular shape,

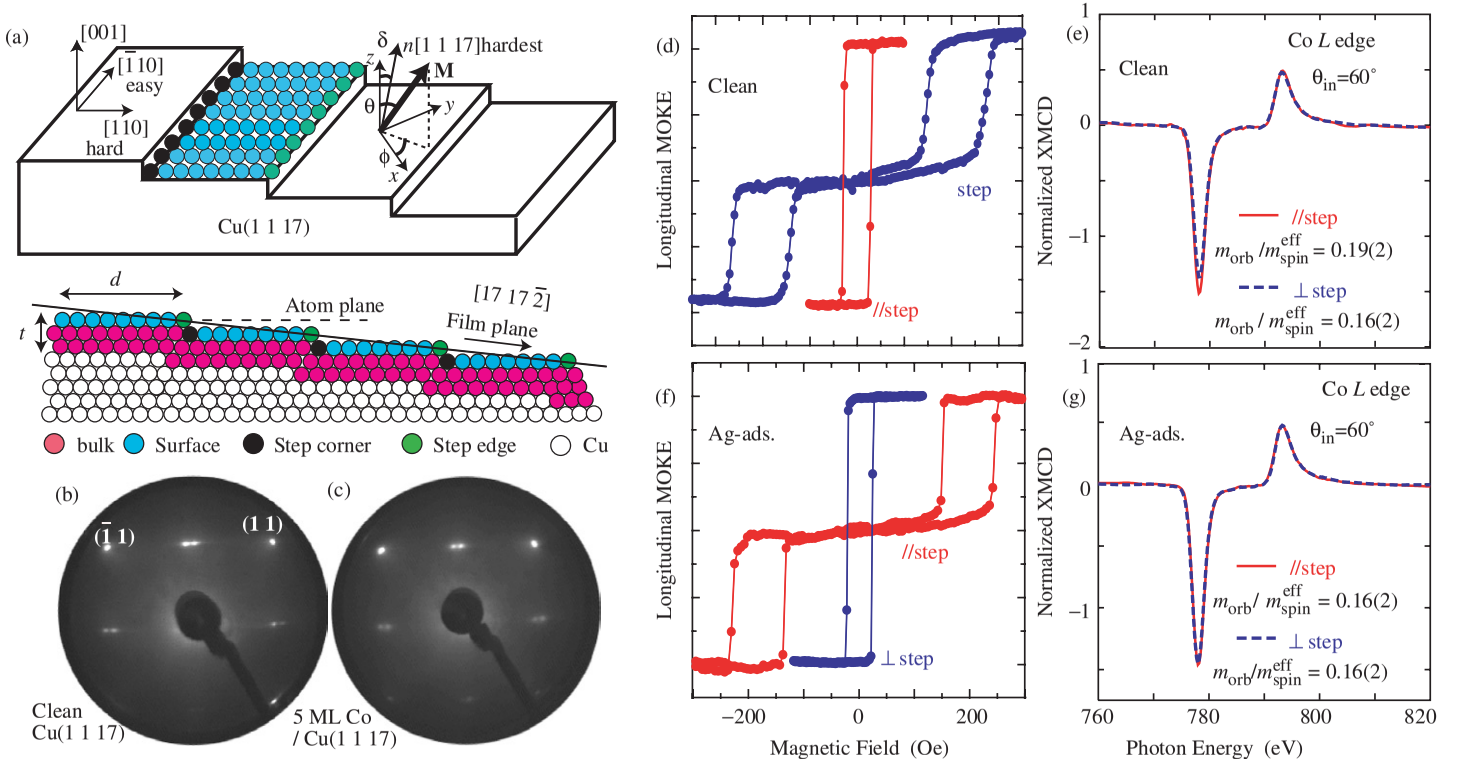

Figure 25. [Colour online] (a) Model surface structure of a Co film on Cu(1 1 17). (b, c) The LEED patterns with the primary electron energy of 127 eV before (b) and after (c) 5 ML Co deposition. The fundamental spots clearly split into two after Co deposition as well, confirming that the Co film grows in a layer-by-layer fashion and the step edge is maintained on the Co film surface. (d) Longitudinal MOKE magnetization hysteresis curves of clean 5 ML Co on Cu(1 1 17) with **H**//step and **H**⊥step. (e) Grazing incidence Co *L*-edge XMCD spectra of clean 3 ML Co on Cu(1 1 17) with **M**//step and **M**⊥step. (f) Longitudinal MOKE magnetization hysteresis curves of 1 ML Ag-deposited 5 ML Co on Cu(1 1 17) with **H**//step and **H**⊥step. (g) Grazing incidence Co *L*-edge XMCD spectra of Ag-deposited 3 ML Co on Cu(1 1 17) with **M**//step and **M**⊥step. From [52].

while the parallel step gives a double hysteresis loop with the shift field of ~200 Oe. This observation implies that the magnetic easy axis is perpendicular to the step within the film plane and that SRT actually occurs upon Ag deposition. Our result confirms the finding by Weber *et al.* [84,85]. Figure 25(g) shows the Co *L*-edge XMCD spectra of Ag(1 ML)/Co(3 ML)/Cu(1 1 17). There can be seen almost no difference between the perpendicular step and parallel step spectra. From the sum rule analysis given in the figure, the ratio of $m_{\mathrm{orb}}/m_{\mathrm{spin}}^{\mathrm{eff}}$ is actually equivalent. When one compares the results with those of the clean ones, one can find that the parallel step orbital magnetic moment is suppressed, while the perpendicular step one is unchanged. Although these results cannot conclude the magnetic easy axis, it is not contradictory to the occurrence of the SRT possibly because the difference is too small to detect by XMCD.

Nakagawa *et al.* [52] further determined the possibility of canted magnetization. Figure 26 shows the incident angle dependence of the Co L_{III}-edge XMCD intensity at the peak top energy. In the case of clean Co, where the magnetic easy axis is along the step edge, the intercept is found at $\theta_{\mathrm{in}} = 0^{\circ}$, in agreement with the fact that the easy axis lies on the film plane with no canting. On depositing Ag, the easy axis turns to the perpendicular step direction even at 0.2 ML Ag, which is approximately equal to the density of the steps. According to Weber *et al.* [85], the Ag atoms adsorb at the step edge and modify the magnetic anisotropy at Co atoms at the step, resulting in the SRT. As the coverage of Ag increases, the intercept is shifted to the negative side that corresponds to the magnetization canting from the film plane to the atom plane. The canting angle at 1 ML Ag is estimated as $\theta = 5.5 \pm 0.5^{\circ}$, which is approximately equivalent to the angle between the film and atom

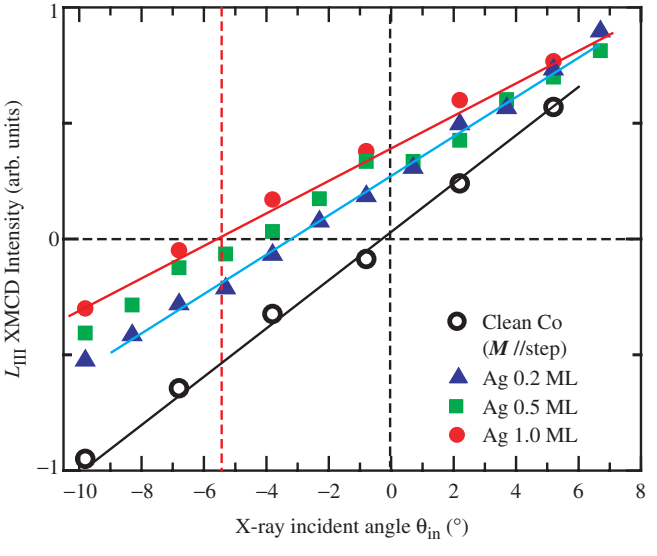

Figure 26. [Colour online] Incident angle dependence of Co L_{III}-edge XMCD at the peak top energy for clean 5 ML Co and Ag (0.2, 0.5 and 1.0 ML)-deposited 5 ML Co on Cu(1 1 17). The angles of 0° and −4.8° correspond to the ones perpendicular to the film and atom plane, respectively. In the case of the clean Co film, the magnetization is parallel to the step edge, while all the Ag-deposited Co films give magnetic easy axes perpendicular to the step. From [52].

planes of 4.76° of Cu(1 1 17). The magnetization thereby is close to the atom plane, and lifted up toward the surface normal direction. In the previous work by Mikuszeit *et al.* [87], it was concluded that the direction of canted magnetization approaches the atomic plane at the thinnest limit, which seems in accordance with the present work.

6.5.3. *NO adsorption on Co/Cu(1 1 17)*

Figure 27(a) shows the magnetic hysteresis curves of the 6 ML Co film after the dosage of a saturated amount of NO at 90 K, recorded with the longitudinal MOKE method. The hysteresis loops are completely identical between the parallel step and perpendicular step directions. The step induced anisotropy vanishes and the film behaves as if the film symmetry is fourfold. Figure 27(b) shows the grazing incidence Co *L*-edge XMCD spectra of NO-adsorbed 6 ML Co on Cu(1 1 17) with **M**//step and **M**⊥step. One can find almost identical XMCD spectra between the two directions. This indicates that the two axes are equivalent, in agreement with the longitudinal MOKE results. Note also that the XMCD intensity is noticeably suppressed compared to those of clean and Ag-deposited films (see Figure 25). We have similarly examined canted magnetization in the NO-adsorbed 5 ML Co film. The measurement method is different from the one in the Ag-deposited film, and the laser excited photoemission MCD was recorded as a function of the incident polar angle θ_{in}. Figure 27(c) gives the incident angle dependence. It is clearly found that the MCD asymmetry vanishes exactly at the normal incidence and that the magnetization is lying on the film plane. The result of the NO adsorbed film is in good contrast to that of the Ag-deposited one.

6.5.4. *Discussion on magnetic anisotropy*

We will finally discuss the magnetic anisotropy observed in the present systems of Ag- and NO-covered Co films on Cu(1 1 17). According to the Néel model [83,88,89], the difference of the magnetic anisotropic energies ΔE_a between **M**//step and **M**⊥step within the film plane is expressed to fourth order as

$$\Delta E_a = -\left(K_{2V} + \frac{K_{2S}}{t} + \frac{K_{2SE}}{tw} + \frac{K_{2SC}}{tw}\right)\sin^2\delta + K_{4V}\sin^4\delta - \frac{K_{4SE}}{tw}(1+\cos^2\delta) + \frac{K_{4SC}}{tw}\sin 2\delta \tag{38}$$

where t is the thickness of the film, w is the width of the terrace, and δ is the angle between the film and atom planes. In the anisotropic constants K, subscripts 2 and 4 denote the second and fourth orders, while subscripts S, V, SE, and SC correspond to the surface, volume, step-edge, and step-corner atoms, respectively [see also Figure 25(a)]. In this equation, since the third term that originates from K_{4SE} (>0) is apparently dominant, the parallel step direction is consequently a magnetic easy axis in clean Co films.

Upon adsorption of NO, the Co film seems to lose twofold step-induced magnetic anisotropy and the magnetic easy axis lies on the film plane as in the clean film. This means that the above ΔE_a is essentially zero. Although the adsorption geometry of NO on stepped Co surfaces is not known, the STM image (not shown) indicates uniform adsorption of NO; NO adsorbs on both the step edge and terrace atoms. Since NO adsorption quenches the orbital magnetic moments of the adsorbed Co atoms, the surface

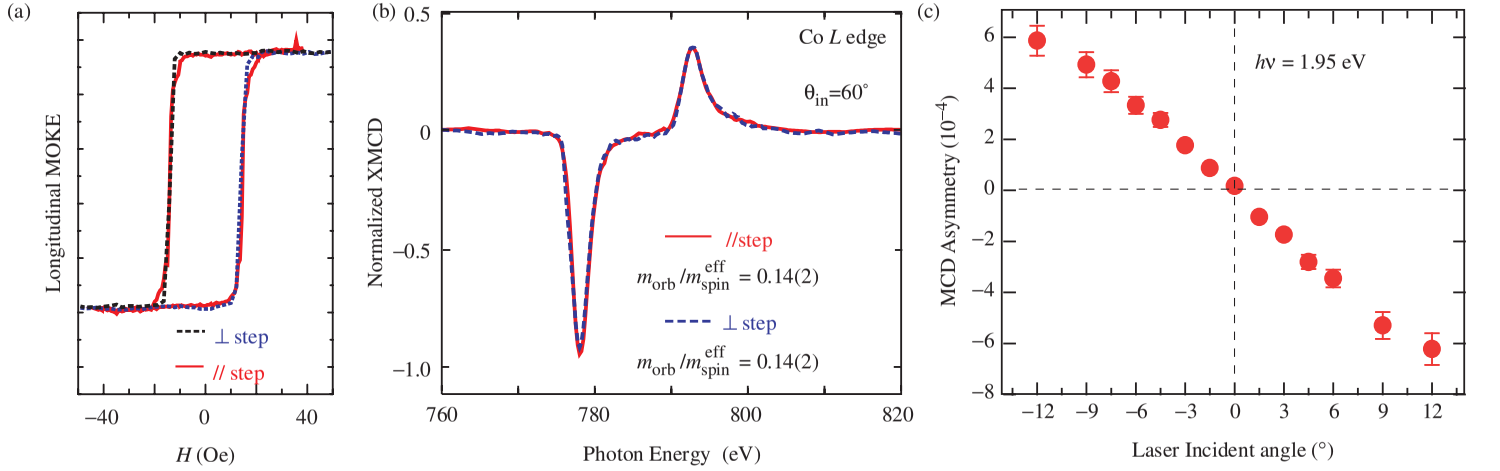

Figure 27. [Colour online] (a) Longitudinal MOKE magnetization hysteresis curves of 3 L NO adsorbed 6 ML Co on Cu(1 1 17) with **H**//step and **H**⊥step. (b) Variation of the shift field as a function of NO exposure. (c) Grazing incidence Co *L*-edge XMCD spectra of NO-adsorbed 6 ML Co on Cu(1 1 17) with **M**//step and **M**⊥step. From [52].

and step edge anisotropies should be suppressed. The present observation of the loss of the step induced anisotropy is thus quite reasonable.

On the other hand, Ag deposition induces the transition of the magnetic easy axis from the parallel step to the perpendicular step direction. Since Ag atoms interact predominantly with the step edge Co atoms, the step edge anisotropy is suppressed, while the step corner anisotropy may be less influenced due to weaker interaction with Ag. This argument can partly explain the SRT. The magnetization is however found to lie closely on the atom plane in Ag/Co/Cu(1 1 17). The energy difference between the **M**//step and **M**⊥step within the atom plane is given as

$$\Delta E_a = -\frac{M_S^2}{2\mu_0}\sin^2\delta - \frac{2K_{4SE}}{tw}. \tag{39}$$

The energy difference is always negative as long as K_{4SE} is positive. Skomski *et al.* [90] discussed unidirectional anisotropy on Co/Cu(1 1 17) based on the experimental observations of the unambiguous unidirectional shift [91,92]. This is not predicted by the Néel model, because the contribution from the step corner atoms is cancelled on the atom plane. The situation of the present observation is quite similar to the previous case and the physical origin of the canted magnetization cannot be explained by the Néel model. In isolated nanowire systems on substrates as well, similar magnetic anisotropy was reported [93,94] and was partly understood theoretically [95]. The one-dimensional Co atomic wires on Pt(997) show an inclined magnetic easy axis. The understanding of the magnetic easy axis of Ag/Co/Cu(1 1 17) needs further quantum-mechanical work.

7. Conclusions and future aspects

In this article, recent technical development of magnetic circular dichroism was reviewed. Spatiotemporal analysis using MCD techniques, which is requested by further improvement of high-density and high-speed recording media in information technology and nanotechnology, has been realized by virtue of technical developments of light sources in lasers and synchrotron radiation and surface analysis tools such as PEEM and SNOM. Although the magneto-optical SNOM technique was not described in this review, the technique [96–99] can be utilized not only for the characterization of nanomagnetism but for magnetic recording itself, and will be further matured and applied to spatiotemporal analysis [100,101]. On the other hand, femtosecond MCD PEEM will be realized in a short period by using ultrashort pulsed UV lasers and X-ray free electron lasers. Femtosecond ultrafast spin dynamics using SNOM and PEEM will be investigated quite soon. Moreover, the time-resolved STM technique [102] will be applied to thin film magnetism in order to achieve abrupt improvement of spatial resolution into atomic scale.

Fabrication of novel magnetic materials is also desired from the view point of surface physical chemistry. For near future GMR/TMR devices, employment of organic films as a nonmagnetic layer may be a good candidate because of high spin coherence due to strong electron–phonon coupling [103–105]. Characterization of electronic as well as structural properties of metal/organic layers will also be substantially important since the morphology of organic molecular crystals should play a definitive role for

high spin coherence. Fabrication of self-assembled nanodots and nanowires on chemically modified surfaces is also attractive [106–109], whose magnetic properties are a very interesting subject in MCD techniques with spatiotemporal resolution.

References

[1] M. N. Baibich, J. M. Broto, A. Fert, *et al.*, Phys. Rev. Lett. **61**, 2472 (1988).
[2] G. Binasch, P. Grünberg, F. Saurenbach, *et al.*, Phys. Rev. **B39**, 4828 (1989).
[3] For instance, see *Handbook of Magnetism and Advanced Magnetic Materials*, Vol. 3 (*Novel Techniques for Characterizing and Preparing Samples*), edited by H. Kronmüller and S. Parkin (John Wiley, Chichester, 2007).
[4] T. Nakagawa and T. Yokoyama, Phys. Rev. Lett. **96**, 237402 (2006).
[5] T. Nakagawa, T. Yokoyama, M. Hosaka, *et al.*, Rev. Sci. Instrum. **78**, 023907 (2007).
[6] G. K. L. Marx, H. J. Elmers, G. Schönhense, *et al.*, Phys. Rev. Lett. **84**, 5888 (2000).
[7] R. Vollmer, Th. Gutjahr-Löser, J. Kirschner, *et al.*, Phys. Rev. **B60**, 6277 (1999).
[8] J. Kerr, Rep. Brit. Assoc. Adv. Sci. **40** (1876).
[9] J. Kerr, Phil. Mag. **3**, 321 (1877).
[10] M. Faraday, Phil. Trans. Roy. Soc. **136**, 1 (1846).
[11] K. W. Hlpps and G. A. Crosby, J. Chem. Phys. **83**, 555 (1979).
[12] K. Sato, Jpn. J. Appl. Phys. **20**, 2403 (1981).
[13] J. Zak, E. R. Moog, C. Liu, *et al.*, Phys. Rev. **B43**, 6423 (1991).
[14] K. Sato, *Magneto-optics* (*Hikari to Jiki*, *in Japanese*) (Asakura, Tokyo, 2001).
[15] H. S. Benett and E. A. Stern, Phys. Rev. **137**, A448 (1964).
[16] P. N. Argyres, Phys. Rev. **97**, 334 (1955).
[17] R. Kubo, J. Phys. Soc. Jpn. **12**, 570 (1957).
[18] Y. Shen, Phys. Rev. **133**, A551 (1964).
[19] F. J. Kahn, P. S. Persian, J. P. Remeika, *et al.*, Phys. Rev. **186**, 891 (1969).
[20] C. S. Wang and J. Callaway, Phys. Rev. **B9**, 4897 (1974).
[21] Z. Q. Qiu and S. D. Bader, Rev. Sci. Instrum. **71**, 1243 (2000).
[22] C. T. Chen, F. Sette, Y. Ma, *et al.*, Phys. Rev. **B42**, 7262 (1990).
[23] J. Stöhr, J. Magn. Magn. Mater. **200**, 470 (1999).
[24] H. Wende, Rep. Prog. Phys. **67**, 2105 (2004).
[25] J. J. Rehr and R. C. Albers, Rev. Mod. Phys. **72**, 621 (2000).
[26] B. T. Thole, P. Carra, F. Sette, *et al.*, Phys. Rev. Lett. **68**, 1943 (1992).
[27] P. Carra, B. T. Thole, M. Altarelli, *et al.*, Phys. Rev. Lett. **70**, 694 (1993).
[28] J. Stöhr and H. König, Phys. Rev. Lett. **75**, 3748 (1995).
[29] P. Bruno, Phys. Rev. **B39**, R865 (1989).
[30] G. van der Laan, J. Phys. Condens. Matter **10**, 3239 (1998).
[31] T. Koide, T. Shidara, H. Fukutani, *et al.*, Rev. Sci. Instrum. **63**, 1462 (1992).
[32] T. Nakagawa, Y. Takagi, Y. Matsumoto, *et al.*, Jpn. J. Appl. Phys., in press.
[33] T. Gejo, Y. Takata, T. Hatsui, *et al.*, Chem. Phys. **289**, 15 (2003).
[34] M. Tischer, O. Hjortstam, D. Arvanitis, *et al.*, Phys. Rev. Lett. **75**, 1602 (1995).
[35] U. Ramsperger, A. Vaterlaus, P. Pfäffli, *et al.*, Phys. Rev. **B53**, 8001 (1996).
[36] O. Hjortstam, J. Trygg, J. M. Wills, *et al.*, Phys. Rev. **B53**, 9204 (1996).
[37] R. Pentcheva and M. Scheffler, Phys. Rev. **B61**, 2211 (2000).
[38] O. Eriksson, A. M. Boring, R. C. Albers, *et al.*, Phys. Rev. **B45**, 2868 (1992).
[39] J. Stöhr, Y. Wu, B. D. Hermsmeier, *et al.*, Science **259**, 658 (1993).
[40] C. M. Schneider, K. Holldack, M. Kinzler, *et al.*, Appl. Phys. Lett. **63**, 2432 (1993).
[41] J. Vogel, W. Kuch, M. Bonfim, *et al.*, Appl. Phys. Lett. **82**, 2299 (2003).

[42] W. Kuch, L. I. Chelaru, K. Fukumoto, *et al.*, Phys. Rev. **B67**, 214403 (2003).
[43] M. Kowalewski, C. M. Schneider, B. Heinrich, *et al.*, Phys. Rev. **B47**, 8748 (1993).
[44] K. Fukumoto, W. Kuch, J. Vogel, *et al.*, Phys. Rev. Lett. **96**, 097204 (2006).
[45] A. Kirilyuk and T. Rasing, Magnetization-induced second harmonic generation, in *Handbook of Magnetism and Advanced Magnetic Materials*, edited by H. Kronmüller and S. Parkin, John Wiley, Chichester, (2007), Vol. 3, pp. 1542.
[46] R.-P. Pan, H. D. Wei, Y. R. Shen, *et al.*, Phys. Rev. **B39**, 1229 (1989).
[47] U. Pustogowa, W. Hübner, K. H. Bennemann, *et al.*, Phys. Rev. **B49**, 10031 (1994).
[48] J. Reif, C. Rau, E. Matthias, *et al.*, Phys. Rev. Lett. **71**, 1931 (1993).
[49] B. Koopmans, M. Groot Koerkamp, Th. Rasing, *et al.*, Phys. Rev. Lett. **74**, 3692 (1995).
[50] G. Spierings, V. Koutsos, H. A. Wierenga, *et al.*, J. Magn. Magn. Mater. **121**, 109 (1993).
[51] K. Sato, A. Kodama, M. Miyamoto, *et al.*, J. Appl. Phys. **87**, 6785 (2000).
[52] T. Nakagawa, H. Watanabe, T. Yokoyama, *et al.*, Phys. Rev. **B74**, 134422 (2006).
[53] C. M. Schneider, M. S. Hammond, P. Schuster, *et al.*, Phys. Rev. **B44**, R12066 (1991).
[54] W. Kuch, A. Dittschar, K. Meinel, *et al.*, Phys. Rev. **B53**, 11621 (1996).
[55] W. Kuch and C. M. Schneider, Rep. Prog. Phys. **64**, 147 (2001).
[56] M. Hosaka, S. Koda, M. Katoh, *et al.*, Nucl. Instrum. Methods **A483**, 146 (2002).
[57] B. Schulz and K. Baberschke, Phys. Rev. **B50**, 13467 (1994).
[58] P. Blaha, K. Schwarz, G. K. H. Madsen, *et al.*, *Computer code WIEN2k* (Technische Universitat Wien, Vienna, 2002).
[59] J. Kuneš, P. Novák, M. Diviš, *et al.*, Phys. Rev. **B63**, 205111 (2001).
[60] P. M. Oppeneer, T. Maurer, J. Sticht, *et al.*, Phys. Rev. **B45**, 10924 (1992).
[61] H. Ebert, Rep. Prog. Phys. **59**, 1665 (1996).
[62] I. D. Moore and J. B. Pendry, J. Phys. **C11**, 4615 (1978).
[63] J. Henk and B. Johansson, J. Electron Specrosc. Relat. Phenom. **94**, 259 (1998).
[64] C. M. Schneider and G. Schönhense, Rep. Prog. Phys. **65**, R1785 (2002).
[65] N. B. Weber, C. Bethke, F. U. Hillebrecht, *et al.*, J. Mag. Mag. Mater. **226**, 1573 (2001).
[66] M. Farle, Rep. Prog. Phys. **61**, 755 (1998).
[67] J. Hong, R. Q. Wu, J. Lindner, *et al.*, Phys. Rev. Lett. **92**, 147202 (2004).
[68] S. van Dijken, R. Vollmer, B. Poelsema, *et al.*, J. Magn. Magn. Mater. **210**, 316 (2000).
[69] D. Sander, W. Pan, S. Ouazi, *et al.*, Phys. Rev. Lett. **93**, 247203 (2004).
[70] B. N. Engel, M. H. Wiedmann, R. A. V. Leeuwen, *et al.*, J. Magn. Magn. Mater. **126**, 532 (1993).
[71] S.-K. Kim and J. B. Kortright, Phys. Rev. Lett. **86**, 1347 (2001).
[72] D. Matsumura, T. Yokoyama, K. Amemiya, *et al.*, Phys. Rev. **B66**, 024402 (2002).
[73] O. Robach, C. Quiros, P. Steadman, *et al.*, Phys. Rev. **B65**, 054423 (2002).
[74] D. Matsumura, K. Amemiya, S. Kitagawa, *et al.*, Phys. Rev. **B73**, 174423 (2006).
[75] S. T. Purcell, M. T. Johnson, N. W. E. McGee, *et al.*, J. Appl. Phys. **73**, 1360 (1993).
[76] J. Chen, M. Drakaki, J. L. Erskine, *et al.*, Phys. Rev. **B45**, 3636 (1992).
[77] X.-D. Ma, T. Nakagawa, T. Yokoyama, *et al.*, Surf. Sci. **600**, 4605 (2006).
[78] P. Ohresser, N. B. Brookes, S. Padovani, *et al.*, Phys. Rev. **B64**, 104429 (2001).
[79] T. Suzuki, M. Kurahashi, Y. Yamauchi, *et al.*, Surf. Sci. **507-510**, 181 (2002).
[80] D. W. Moon, S. Cameron, F. Zaera, *et al.*, Surf. Sci. **180**, L123 (1987).
[81] R. S. Saiki, G. S. Herman, M. Yamada, *et al.*, Phys. Rev. Lett. **63**, 283 (1989).
[82] A. Berger, U. Linke, H. P. Oepen, *et al.*, Phys. Rev. Lett. **68**, 839 (1992).
[83] D. S. Chuang, C. A. Ballentine, R. C. O'Handley, *et al.*, Phys. Rev. **B49**, 15084 (1994).
[84] W. Weber, C. H. Back, A. Bischof, *et al.*, Nature (London) **374**, 788 (1995).
[85] W. Weber, C. H. Back, U. Ramsperger, *et al.*, Phys. Rev. **B52**, R14400 (1995).
[86] S. S. Dhesi, G. van der Laan, E. Dudzik, *et al.*, Phys. Rev. Lett. **87**, 067201 (2001).
[87] N. Mikuszeit, S. Pütter, H. P. Oepen, *et al.*, J. Magn. Magn. Mater. **268**, 340 (2004).
[88] L. Néel, J. Phys. Radium **15**, 225 (1954).

[89] S. Chikazumi and C.D. Graham Jr, *Physics of Ferromagnetism*, 2nd ed. (Oxford University Press, Oxford, 1997).
[90] R. Skomski, H. P. Oepen, J. Kirschner, *et al*., Phys. Rev. B **58**, 11138 (1998).
[91] W. Wulfhekel, S. Knappmann, B. Gehring, *et al*., Phys. Rev. B **50**, 16074 (1994).
[92] W. Wulfhekel, S. Knappmann, H. P. Oepen, *et al*., J. Appl. Phys. **79**, 988 (1996).
[93] P. Gambardella, A. Dallmeyer, K. Maiti, *et al*., Nature (London) **416**, 301 (2002).
[94] P. Gambardella, A. Dallmeyer, K. Maiti, *et al*., Phys. Rev. Lett. **93**, 077203 (2004).
[95] J. Dorantes-Dávila and G. M. Pastor, Phys. Rev. Lett. **81**, 208 (1998).
[96] E. Betzig, J. K. Trautman, R. Wolfe, *et al*., Appl. Phys. Lett. **61**, 1432 (1992).
[97] E. Betzig, J. K. Trautman, J. S. Weiner, *et al*., Appl. Opt. **31**, 4563 (1992).
[98] T. Ishibashi, T. Yoshida, J. Yamamoto, *et al*., J. Magn. Soc. Jpn. **23**, 712 (1999).
[99] T. Ishibashi, T. Yoshida, A. Iijima, *et al*., J. Microscopy **194**, 374 (1999).
[100] T. Nagahara, K. Imura, H. Okamoto, *et al*., Rev. Sci. Instrum. **75**, 4528 (2004).
[101] K. Imura, T. Nagahara, H. Okamoto, *et al*., J. Phys. Chem. **B109**, 13214 (2005).
[102] S. Yoshida, Y. Kanitani, R. Oshima, *et al*., Phys. Rev. Lett. **98**, 026802 (2007).
[103] V. Dediu, M. Murgia, F. C. Matacotta, *et al*., Solid State Comm. **122**, 181 (2002).
[104] Z. H. Xiong, D. Wu, Z. V. Vardeny, *et al*., Nature **427**, 821 (2004).
[105] H. Wende, M. Bernien, J. Luo, *et al*., Nature Mater. **6**, 516 (2007).
[106] T. M. Parker, L. K. Wilson, N. G. Condon, *et al*., Phys. Rev. **B56**, 6458 (1997).
[107] F. Komori, K. D. Lee, K. Nakatsuji, *et al*., Phys. Rev. **B63**, 214420 (2001).
[108] X. D. Liu, B. Lu, T. Iimori, *et al*., Phys. Rev. Lett. **98**, 066103 (2007).
[109] S. M. York and F. M. Leibsle, Phys. Rev. **B64**, 033411 (2001).